Midbrain stimulation in freely behaving mice by photothermal transducers actuated via widefield near-infrared II light

Xiang Wu[1,3,&],

Yuyan Jiang[4,&],

Nicholas J. Rommelfanger[2,3],

Fan Yang[1,3],

Qi Zhou[1,3],

Rongkang Yin[1,3],

Junlang Liu[1,3],

Sa Cai[1,3],

Wei Ren[1,3],

Andrew Shin[1],

Kyrstyn S. Ong[1,3],

Kanyi Pu[4,5,*],

Guosong Hong[1,3,*]

[1]Department of Materials Science and Engineering, Stanford University, Stanford, California, 94305, USA

[2]Department of Applied Physics, Stanford University, Stanford, California, 94305, USA

[3]Wu Tsai Neurosciences Institute, Stanford University, Stanford, California, 94305, USA

[4]School of Chemical and Biomedical Engineering, Nanyang Technological University, 70 Nanyang Drive, Singapore 637457, Singapore

[5]Division of Chemistry and Biological Chemistry, School of Physical and Mathematical Sciences, Nanyang Technological University, 21 Nanyang Link, Singapore 637371, Singapore

[*]Corresponding authors, guosongh@stanford.edu; kypu@ntu.edu.sg.
[&]These authors contributed equally

Abstract

Invasive brain implants and tethered optical fibres are typically used in restrained or motion-impaired animals, limiting the control and the decoding of the neural circuitry in freely behaving ones. Here we report the implant- and tether-free optical neurostimulation of deep brain regions by locally injected and untargeted photothermal transducers. The macromolecular transducers, comprising a semiconducting polymer core and an amphiphilic polymer shell, have an average diameter of 40 nanometres and achieve a photothermal conversion of 71% (at 1064 nm), activating the transient receptor potential cation channel subfamily V member 1 (TRPV1) ectopically expressed by an adeno-associated virus in dopaminergic neurons of tyrosine hydroxylase-driven Cre recombinase transgenic mice. The near-transparency of biological tissue in the second near-infrared window enabled the light source to be placed at 50 centimetres above the mouse, at a low incident power density of 10 milliwatt/square millimetre, resulting in the activation, through the scalp and skull, of the dopaminergic neurons in the ventral tegmental area, with minimal thermal damage. The approach is suitable for the neurostimulation of socially interacting mice.

Understanding complex neural circuitry and its correlation to specific behaviours requires spatially and temporally precise modulation of neuron subtypes in certain brain regions[1–3]. For decades, neural stimulation has been predominantly achieved with traditional electrical stimulation electrodes[4]. More recently, optogenetics has gained great popularity due to its rapid control of neural activities with visible light and its dissection of neural circuitry by selectively modulating specific neuron subtypes[1–3]. Alternatively, non-genetic optical neural interfaces have also been developed to allow neural stimulation with high spatiotemporal resolution[5–7].

However, deep-brain neural modulation usually involves invasive implantation of stimulation electrodes and optical fibres due to the screening of electric fields and the scattering of light in the brain tissue[8–10]. Chronic brain implants lead to permanent damage to the brain tissue and overlying skull/scalp, while inducing a chronic immune response at the implant/tissue interface[10,11]. Furthermore, tethering the animal to an electrical wire or an optical fibre during behavioural studies leads to various deleterious consequences, especially for socially interacting animals (Supplementary Table 1)[3,12]. To mitigate these challenges, several novel methods have been demonstrated, including wireless optogenetic interfaces[3,13], red-shifted opsins[14–18], ultrasensitive opsins[18–20], optogenetic antennas based on upconversion micro/nanoparticles[21,22], and sono-optogenetics based on mechanoluminescent nanoparticles[23]. Despite these recent advances, none of the existing optogenetic interfaces are able to altogether eliminate both the head tethering/fixing and the brain implants for deep-brain neural modulation in freely moving animals[13,21]. Magnetothermal neural modulation has been shown to free the animals from both head tethering and brain implants, yet it still requires a strong magnetic field provided by a resonant coil in close vicinity to the subject's head[24,25]. A noninvasive alternative is chemogenetics via peripherally or orally administered chemical actuators for selectively activating ligand receptors. However, chemogenetic neuromodulation has coarse temporal resolution due to the long residence time of chemical actuators *in vivo*[26,27]. Therefore, it is desirable to develop new methods that can modulate neural activity in the deep-brain

regions of naturally behaving animals with high temporal resolution via a tether-free and implant-free interface.

Here, we report macromolecular infrared nanotransducers for deep-brain stimulation (MINDS) in freely behaving animals through the scalp and skull. MINDS can absorb light in one of the biological transparency windows, the second near-infrared window (NIR-II window, 1000–1700 nm; Fig. 1a)[28], modulating neural activity via temperature-sensitive transient receptor potential (TRP) channels[29,30]. We demonstrate through-scalp deep-brain optical neuromodulation in fibre-free and naturally-behaving animals with distant NIR-II illumination from >50 cm above the mouse head at a low incident power density of up to 10 mW mm^{-2}. Our approach could open opportunities for stimulating an animal in a socially interacting environment by remotely irradiating NIR-II light.

Results

We rationally chose 1064-nm light, since it offers the greatest tissue penetration by reduced scattering and similar, if not less, absorption in the brain tissue compared to visible light. In addition, 1064-nm light exhibits significantly lower water absorption than the longer-wavelength NIR-II spectrum beyond 1100 nm. We estimated the combined effect of scattering and absorption by calculating the brain effective attenuation spectrum (Supplementary Fig. 1) and found that the 1064-nm wavelength is located near the global minimum of the brain tissue attenuation spectrum in the entire 400–1800 nm range, which was validated by a previous report on light-tissue interaction[31]. Another advantage of 1064 nm, compared to other wavelengths around the attenuation spectral minimum, comes from its wide availability afforded by Nd:YAG lasers.

Owing to the minimum attenuation of 1064-nm light in the brain, it can penetrate to deeper brain regions than shorter wavelengths in the visible and traditional near-infrared (NIR-I, 700–900 nm) windows. Monte Carlo simulation reveals that 1064-nm NIR-II light can penetrate to a depth of at least 5 mm in the brain through the scalp and skull (Supplementary Fig. 2). In contrast, 635-nm visible light or 980-nm NIR-I light is absorbed more by the scalp and the brain surface non-specifically, resulting in lower energy reaching the deep brain (Supplementary Fig. 2). Therefore, although transcranial deep-brain optogenetics has been reported, existing techniques operated in the visible and NIR-I windows still require skull-tethered optical fibres to deliver light at a high incident power density to compensate for the loss in the brain[18,21].

Design principles and photothermal performance of MINDS.

MINDS were designed with a π-conjugated semiconducting polymer core of pBBTV (poly(benzobisthiadiazole-*alt*-vinylene); Supplementary Fig. 3,4) to afford efficient absorption of 1064-nm light. This polymer core was coated with an amphiphilic and FDA-approved polymer shell, poly(lactide-co-glycolide)-*b*-poly(ethylene glycol) (PLGA-PEG; Fig. 1b) to afford water solubility and biocompatibility. MINDS have an average diameter of ~40 nm, as revealed by transmission electron microscopy (TEM, Fig. 1c) and dynamic light scattering (DLS, Fig. 1d).

MINDS have the following four key design principles that make them efficient NIR-II sensitizers to activate TRPV1 channels *in vivo*. First, MINDS are strong NIR-II light absorbers: the pBBTV core of the MINDS has strong absorption in the > 1000 nm NIR-II window (Fig. 1e) via adjustment of the highest occupied and the lowest unoccupied molecular orbitals (HOMO-LUMO) of the donor and acceptor units. Second, MINDS are efficient heat generators upon NIR-II illumination: under continuous 1064-nm illumination at 10 mW mm^{-2}, 1.8 mg mL^{-1} MINDS solution reached 39 °C within merely 1.1 s (Fig. 1f,g). Specifically, the photothermal conversion efficiency of MINDS at 1064 nm was measured to be 71% (Methods), which represents one of the highest photothermal conversion efficiencies in the NIR-II window (Supplementary Table 2). Continuous 1064-nm illumination of human embryonic kidney (HEK) 293T cell pellets after incubation with MINDS resulted in significantly greater heating than the control group without MINDS (Fig. 1h). Third, MINDS remain stable in normal physiological condition and demonstrate superior photostability upon repeated NIR-II illumination. The structural stability of MINDS has been confirmed by the minimal change in either optical absorption or the hydrodynamic diameter over 7 days of incubation in phosphate buffered saline (PBS) and cell culture medium at 37 °C (Supplementary Fig. 5). Furthermore, the *in vivo* photostability of MINDS was proved by negligible variation in the photothermal performance for more than 70 heating/cooling cycles over 1 h (Supplementary Fig. 6). Fourth, the organic semiconducting polymer core and the PLGA-PEG shell render MINDS biocompatible. Compared to inorganic gold nanoparticles, organic semiconducting polymers have been reported to afford low toxicity and rapid biodegradation[32]. Primary neuron culture showed no reduction in cell viability after 24 h of incubation with MINDS up to a concentration of 3.6 mg mL^{-1} (Supplementary Fig. 7), while only a minimal chronic immune response was observed in the brain tissue near the injection sites of MINDS when compared with the carrier injection (Supplementary Fig. 8).

The superior photothermal performance of MINDS allows them to transfer heat to ectopically expressed TRP channels in neurons. Infrared-sensitive species such as venomous pit vipers sense long-wavelength radiation (750 nm – 1 mm) using TRP channels in a specialized organ[33]. More recently, ectopic expression of TRPV1 channels in mouse retinal cones endows vision in the infrared via the resonant absorption of gold nanorods[29]. Based on these results, we hypothesize that ectopic expression of TRPV1 channels in the mouse brain coupled with 1064-nm absorbing MINDS can achieve deep-brain neuromodulation with brain-penetrant NIR-II light. Several previous reports have used physical targeting of heat-producing nanoparticles to TRP channels and cell membranes[24,29,34]. However, we used untargeted MINDS for activating TRPV1 under NIR-II illumination in the following experiments, because the temporal dynamics of TRPV1 activation precludes the need for physically binding MINDS to TRPV1 channels. The fastest reported time constant of TRPV1 activation is 5 ms, achieved under a high laser power density of 1.0×10^6 mW mm^{-2} to drive rapid temperature increase (Supplementary Table 3)[35]. Based on the Fourier heat equation, a thermal diffusion length of ~50 μm is expected over this timescale, much greater than the size of a neuron and its membrane. Similarly, a recent study rejects the existence of nanoscale heat confinement on the surface of particles[36]. Therefore, we reason

that untargeted MINDS can provide sufficient heat diffusion to activate TRPV1 channels for both *in vitro* and *in vivo* experiments below.

In vitro NIR-II photothermal activation of TRPV1 with MINDS.

We then asked if focused NIR-II illumination was able to activate TRPV1 in the presence of MINDS. TRPV1 functions as a nonselective cation channel with a high permeability to calcium when activated[37]. Therefore, we used calcium imaging to demonstrate NIR-II activation of TRPV1 channels in HEK293T cells (Fig. 2a), which were transfected with pAAV-CMV-TRPV1-mCherry plasmids. Dynamic calcium imaging upon 1040-nm NIR-II illumination (parameters summarized in Supplementary Table 3 and Methods) revealed several key findings.

First, the specificity of calcium signal increase in MINDS+ and TRPV1+ cells suggests that MINDS-sensitized TRPV1 channels are activated under NIR-II illumination. $62.5 \pm 17.3\%$ of MINDS+/TRPV1+ cells responded to NIR-II stimulation with a more than 4-fold increase in calcium fluorescence intensity. In contrast, only < 1.5% of the cells in any control group showed a similar response within 5 s of NIR-II illumination, indicating the necessity of both MINDS and TRPV1 to increase the intracellular calcium concentration by NIR-II (Fig. 2b–d). We then proved that the observed calcium transients were neither from intracellular release of Ca^{2+} ions from endoplasmic reticulum calcium stores[38] nor membrane capacitive current[5,39,40]. Specifically, TRPV1– cells showed no increase in calcium fluorescence even in the presence of MINDS upon NIR-II illumination (Fig. 2b–d). Furthermore, the cell specificity for NIR-II activation was confirmed by the colocalization of calcium signal increase and TRPV1 expression (Supplementary Fig. 9). In addition, MINDS– cells showed little calcium increase, suggesting that heat transfer to ectopically expressed TRPV1 channels via direct NIR-II illumination is inefficient and requires higher intensities of photon flux that would damage the neural tissue[29]. Therefore, the strong absorption of NIR-II light by MINDS sensitizes TRPV1 to low-intensity NIR-II light for neuromodulation.

Second, temporal dynamics of calcium signals in multiple cells suggested an average response time of 0.9 ± 0.2 s (Fig. 2e; Supplementary Table 3). It has been reported that TRPV1 can be activated by a temperature jump on a millisecond timescale[35]. Therefore, the temporal response of our photothermal TRPV1 activation method should be dependent on the rate of temperature increase, which in turn depends on the power density of the NIR-II illumination. In our cell experiments where an average response time of 0.9 ± 0.2 s was found (Fig. 2e), we used a laser power density of 400 mW mm^{-2}, much lower than that of 10^5-10^6 mW mm^{-2} in previous reports with ~ms temporal dynamics for activating TRPV1 (Supplementary Table 3)[35]. Thus, a longer response time is anticipated for *in vivo* photothermal neuromodulation due to a more stringent constraint on the allowable power density of NIR-II illumination on the animals.

In vivo NIR-II neural stimulation in the mouse hippocampus and motor cortex.

Having demonstrated selective activation of MINDS-sensitized TRPV1 with NIR-II illumination *in vitro*, we asked if MINDS allowed for neural activation and behavioural

modulation of live mice *in vivo*. A power density of 8 mW mm^{-2} within the safety limit was used for the 1064 nm illumination[41]. To avoid overheating the scalp and the brain with the NIR-II light, a thermal camera was used to monitor the temperature of the scalp (Supplementary Fig. 10) during the experiment, and a discontinuous illumination protocol with feedback control was applied to activate TRPV1 with a temperature increase from 37 °C to 39 °C (Methods)[42]. Real-time scalp temperature measurements with the thermal camera and Monte Carlo simulation (Methods) revealed that the temperature in the target brain region oscillates around 39 °C with an overshoot of   1.2 °C. Moreover, a temperature increase of 2 °C was sufficient to partially activate TRPV1 expressed in the neuron membranes (Supplementary Note 1).

We first examined whether NIR-II neuromodulation would be sufficient to activate neural activity *in vivo*. A viral vector with a pan-neuronal promoter eSyn (AAV5-eSyn-TRPV1-p2A-mCherry) was stereotactically injected into the mouse hippocampus for transduction of neurons with TRPV1, followed by the injection of MINDS in the same region 3~4 weeks later (see Methods). *In vivo* electrophysiological recording was performed in anaesthetized mice immediately after injection of MINDS. The hippocampus was chosen for recording due to the relatively high neuron soma density in CA1 that affords straightforward measurement of extracellular action potentials[43]. Recordings in the TRPV1+/MINDS+ mouse brain showed a statistically significant increase in neuron firing rate upon NIR-II illumination in a reproducible manner, compared to the control groups that lack TRPV1 or MINDS (Fig. 3a and Supplementary Fig. 11). This lack of a significant change in firing rate of the TRPV1–/MINDS+ group ruled out the possibility of non-specific neuron modulation directly through the membrane capacitive current or inwardly rectifying K$^+$ channels driven by the temperature increase[40,44]. Additionally, a similar baseline firing rate without NIR-II illumination between TRPV1+ (5.5 Hz) and TRPV1– groups (6.3 Hz) suggests minimal adverse effects of ectopic TRPV1 expression to the neuron's excitability. Similarly, a comparable baseline firing rate between MINDS+ (5.5 Hz) and MINDS– groups (6.4 Hz) suggests minimal adverse effects to the neuron's firing ability due to the presence of MINDS.

We then hypothesized that NIR-II illumination was able to activate motor cortex neurons through the scalp and induce unilateral circling of freely behaving animals (Fig. 3b). The lack of any brain implants or head tethering, and the use of distant NIR-II light to track the mouse head, should eliminate any perturbation to the natural behaviour of freely moving animals within the arena (Fig. 3c and Supplementary Table 1). To this end, we performed unilateral transduction of neurons in the secondary motor cortex (M2)[24,45] using the AAV5-eSyn-TRPV1-p2A-mCherry virus, followed by the injection of MINDS in the same region 3~4 weeks later (Fig. 3d). The synapsin promoter was used in a recent study of magnetothermal deep brain stimulation to drive unilateral circling by stimulating the secondary motor cortex[24]. Distant 1064-nm illumination, invisible to the subject and targeted to the head, was able to penetrate through the scalp and skull for modulating MINDS-sensitized M2 neurons of the mouse without any fibre implants or tethering in a rectangular arena (Fig. 3c; see Methods).

Behavioural experiments demonstrated that NIR-II light effectively induced unilateral circling behaviour, as evidenced by the contrast between the random exploratory trajectories without NIR-II light and unilateral circling behaviour during NIR-II illumination (Supplementary Movie 1 and Fig. 3e). NIR-II neuromodulation has a key advantage over conventional optogenetics for modulating motor activity, since it frees the animals from any permanent brain implant or fibre tethering (see Discussion for comparison). Furthermore, compared to magnetothermal stimulation where the magnetic coil limits the arena to roughly the size of the animal[24], distant NIR-II illumination enables a much larger arena for animal behavioural study without any size constraints.

It is important to evaluate the temporal kinetics of *in vivo* NIR-II neuromodulation. From the behavioural study of NIR-II induced unilateral circling, an average latency time of 5.0 ± 1.5 s (mean ± 1 SD; Fig. 3f,g) was found under a power density of 8 mW mm^{-2} at 1064 nm. A similar latency time of ca. 2.9 s, which was defined as the time it took for the firing rate to increase by 50% of the baseline[25], was found from *in vivo* electrophysiological recordings at the same power density (Supplementary Fig. 11e). As discussed above, the temporal resolution of our method depends on the power density of NIR-II illumination. Despite the ~ms response time under a power density of 10^5-10^6 mW mm^{-2} in previous reports (Supplementary Table 3)[35] and the response time of 0.9 ± 0.2 s under a power density of 400 mW mm^{-2} in our *in vitro* experiments (Fig. 2e), *in vivo* application of NIR-II illumination should follow strict guidelines on the limits of exposure to the laser to prevent any thermal damage to the brain[41]. Specifically, for NIR-II neuromodulation in the M2, a power density of 8 mW mm^{-2} was used, 50× lower than used *in vitro*, thereby leading to a longer response time. The ~5 s latency time also agrees with temperature in the M2, which increased to 39 °C within 2 s of NIR-II illumination (Supplementary Fig. 12a,b). The difference between the temperature dynamics and the latency time measured from behavioural experiments could be attributed to the delay between the temperature increase and the ramp of neural activity to reach the threshold, and the delay between neural activation and the onset of behavioural response[46].

Besides the onset time of *in vivo* NIR-II photothermal activation, we also measured the offset time and compared it with similar methods. Electrophysiological measurements revealed an offset time of 8.6 s, which was defined as the time it took for the firing rate to drop below 50% above the baseline (Supplementary Fig. 11e). A similar offset time of 10.7 s was found from behavioural experiments when the NIR-II light was turned off (Fig. 3f). The offset time is shorter than that of magnetothermal stimulation (14.7 s)[24] as heat diffusion is more spatially confined with a shorter onset time, thus leading to more rapid cooling. Moreover, the offset time of photothermal neuromodulation is much shorter than that of chemogenetics (hours), which is limited by slow clearance and regenerative downstream events of designer drugs (e.g., CNO and varenicline)[26,27].

We next demonstrated the necessity of ectopically expressed TRPV1 for *in vivo* NIR-II neuromodulation. First, immunohistochemical staining of TRPV1 in the M2 region of the wild-type mouse brain revealed low endogenous expression of TRPV1 (Fig. 4a). Second, we have carried out *in vivo* electrophysiological, behavioural, and immunohistological studies to compare a group of TRPV1+/MINDS+ animals ($n = 11$) with another group of TRPV1–/

MINDS+ animals ($n = 9$). We hypothesized that these two groups of animals would show no statistically significant difference in these studies if the endogenously expressed TRPV1 or other temperature-sensitive ion channels suffice in driving the NIR-II photothermal neuromodulation in the presence of MINDS. The recorded neuron firing rate change upon NIR-II illumination in the TRPV1–/MINDS+ group is significantly smaller than that in the TRPV1+/MINDS+ group (P < 0.001; Supplementary Fig. 11c). Furthermore, we have also verified the specific activation of M2 neurons with ectopically expressed TRPV1 in the presence of MINDS by immunohistological staining for c-Fos, an immediate early gene for labelling neuronal activity (Fig. 4)[25]. A significant increase in the number of c-Fos-positive cells was only observed in the TRPV1-overexpressed mice with MINDS injection after NIR-II illumination, but not in any of the control groups. In addition, mice in the TRPV1+/MINDS+ group exhibited a significant increase in rotation speed (4.60 rev min^{-1}) upon NIR-II illumination, which was not observed in the TRPV1–/MINDS+ group (*P* < 0.0001; Fig. 3h). The behavioural results also help rule out the possibility that other TRPV1-expressing neurons outside the brain, such as the dorsal root ganglion neurons receiving sensory inputs from the peripheral nervous system (PNS)[47], drove the observed unilateral rotation due to the diffusion of brain-injected MINDS to the PNS. Furthermore, when NIR-II irradiation was off, TRPV1+ animals do not show a statistically significant difference (P > 0.05) in the rotation behaviour (characterized as the angular speed) from TRPV1–control groups (Fig. 3h). This lack of significant difference verifies a negligible effect of ectopic TRPV1 expression alone on the animals' rotation behaviours. Taken together, these results confirmed the selective NIR-II stimulation of ectopically TRPV1-expressing neurons in the M2.

We then investigated the necessity of MINDS for *in vivo* NIR-II neuromodulation. First, M2 temperature increased to 39 °C with a spatially confined distribution around the MINDS injection site after ca. 2 s of NIR-II illumination, whereas it only increased 0.2 °C after the same illumination duration without MINDS (Supplementary Fig. 12b). The spatially confined temperature increase has been verified by both experiments (Supplementary Fig. 10, 12e,f) and simulation (Supplementary Fig. 12a). These results indicate the superior photothermal performance of MINDS over normal brain tissue. Second, we carried out *in vivo* electrophysiological, behavioural, and immunohistological studies to test whether direct NIR-II illumination without MINDS can activate TRPV1 in the brain. We found that the change of neuron firing rates upon NIR-II illumination in the TRPV1+/MINDS– group is significantly smaller than that in the TRPV1+/MINDS+ group (P < 0.001; Supplementary Fig. 11c). Additionally, the significant increase in rotation speed of mice in the TRPV1+/MINDS+ group upon NIR-II illumination was not found in the TRPV1+/MINDS– group under the same experimental conditions (*P* < 0.0001; Fig. 3h). Moreover, immunohistological imaging revealed little c-Fos expression in TRPV1+ neurons in the absence of MINDS (Fig. 4). Therefore, the strong absorption of NIR-II light by MINDS sensitizes TRPV1 to low-intensity NIR-II illumination for neuromodulation. In summary, a significant increase in the neuron firing rate, mouse rotation speed, and the number of c-Fos-positive cells was only observed in the TRPV1+/MINDS+ mice after NIR-II illumination, but not in any of the control groups (Supplementary Fig. 11c&e, Fig. 3h&4b). Together

these data demonstrate that both TRPV1 and MINDS are essential for effective and selective NIR-II photothermal stimulation to modulate animal motor behaviours.

NIR-II deep-brain stimulation.

We next investigated whether NIR-II light can penetrate deep enough to stimulate neural activity in deep-brain regions. We chose the VTA as our target owing to its deep location inside the brain and its pivotal role in the brain's reward circuitry that could be studied with a conditioned place preference test (Fig. 5a)[2]. It has been demonstrated that optogenetic activation of VTA dopaminergic neurons induces real-time place preference, yet an invasive brain implant or a tethered optical fibre is typically required for light delivery in this deep brain region[2,13,18]. We selectively tagged dopaminergic neurons in the VTA by using an AAV virus (AAV5-EF1α-DIO-TRPV1) encoding TRPV1 in a double-floxed inverted open reading frame (DIO) in tyrosine hydroxylase (TH)-driven Cre recombinase (TH-Cre) transgenic mice (Fig. 5b)[13]. The Cre-dependent specific expression of TRPV1 in VTA dopaminergic neurons was confirmed by the colocalization of TH and TRPV1 (Fig. 6). After injecting MINDS in the VTA, we performed contextual conditioning for normally behaving animals in a Y-maze by associating a specific grating pattern at one of the arm terminals with widefield NIR-II illumination (red dashed square, Fig. 5c; Supplementary Fig. 13). Due to the deep location of VTA in the brain, a power density of 10 mW mm^{-2}, slightly higher than that used in the M2 (8 mW mm^{-2}) but still within the safety limit[41], was applied. Real-time scalp temperature measurements with the thermal camera and Monte Carlo simulation revealed that the temperature in the target brain region was stabilized within 39.1 ± 0.7 °C (mean ± maximum absolute deviation), facilitated by the closed-loop feedback control (Methods).

After contextual training with NIR-II neuromodulation on three consecutive days[13], mice with both TRPV1 transduction and MINDS injection in VTA demonstrated strong preference in the NIR-II illuminated arm terminal, as evidenced by longer time the mice spent therein in the post-test (Fig. 5d, Supplementary Fig. 14 and Supplementary Movie 2,3). This result proves deep-brain optical neuromodulation without using any optical fibres in freely behaving animals. Furthermore, the specificity of *in vivo* NIR-II neuromodulation of VTA neurons was validated by comparing the TRPV1+/MINDS+ group with the control groups, in which the animals missed TRPV1 transduction, or MINDS injection, or both (Fig. 5e,f).

We first confirmed the selective NIR-II stimulation of ectopically TRPV1-expressing dopaminergic neurons in the VTA. Importantly, immunohistochemical staining of TRPV1 in the VTA region of the non-transduced brain revealed low endogenous expression of TRPV1 in the TH+ neurons (Fig. 6a). Similar to NIR-II neuromodulation in the M2, endogenous TRPV1 expression in other parts of the brain or in the PNS could have led to the observed place preference. However, the demonstrated place preference in the TRPV1+/MINDS+ group was not found in the TRPV1–/MINDS+ group, with a statistically significant difference between the groups (Fig. 5e,f). In addition, we found no statistically significant difference in the preference score between TRPV1+/MINDS– and TRPV1–/MINDS– groups, thus confirming the lack of any behavioural effect due to the ectopic

TRPV1 expression alone in dopaminergic neurons in the VTA. Furthermore, we have also verified the specific activation of dopaminergic, TH+ neurons with ectopically expressed TRPV1 by immunohistological staining for c-Fos, which was not found for TH+ neurons lacking TRPV1 overexpression (Fig. 6a&b). Finally, the non-specific heating of the neural tissue, especially the tissue above the VTA due to proximity to the NIR-II light, only led to a small temperature increase to 37.9 °C. A similar temperature increase was found for in-vivo optogenetic stimulation with a minimal light power and duration that does not produce thermal modulation of behavior[44]. We have independently verified that non-specific heating of the brain tissue induced negligible change of firing rates of TRPV1– neurons (Supplementary Fig. 11), which has also been confirmed in previous magnetothermal neural stimulation reports[24,25].

We next sought to prove the necessity of MINDS to sensitize the ectopically expressed TRPV1 receptors under NIR-II. First, the superior photothermal performance of MINDS and deep penetration of 1064-nm light resulted in a local hot spot around the MINDS injection site deep inside the brain (Supplementary Fig. 12c,e,f). Second, we have found that without MINDS, the VTA temperature only increased by 0.5 °C, in contrast to 2.1 °C with MINDS over the same NIR-II illumination condition (Supplementary Fig. 12c,d). Third, the results of behavioural experiments demonstrated negligible place preference in the two MINDS– groups (Fig. 5e,f). Finally, immunohistological staining of VTA brain slices revealed a significantly lower percentage of c-Fos+ cells out of all TRPV1+ neurons without MINDS (Fig. 6c).

Given the importance of MINDS for NIR-II sensitization, we also evaluated the *in vivo* distribution and potential long-term utility of MINDS. In order to visualize the *in vivo* distribution and cellular uptake of MINDS, we doped a green fluorescence dye 1-chloro-9,10-bis(phenylethynyl)anthracene into MINDS and named the complex 'MINDS-Fluor' (Methods). Although most of MINDS remained in the extracellular space, some of them were internalized by neurons and glia. Specifically, we found MINDS inside neuron somata, neurites, and the cell body of astrocytes and microglia (Supplementary Fig. 15,16). This finding agrees with a previous report of neuronal uptake of nanoparticles with similar sizes[48]. We have also verified that MINDS remained functionally stable *in vivo* and still demonstrated superior differential heating over normal brain tissue for at least 2 weeks after injection (Supplementary Fig. 17), indicating its potential for long-term utility. Additionally, our preliminary data shows that MINDS with an amount as low as 0.3 μg is sufficient to significantly elevate the c-Fos expression level in the M2 after 8 mW mm^{-2} NIR-II illumination when compared with the MINDS (–) control, which might be utilized in future studies for less invasive delivery of MINDS. Furthermore, thermal damage to the brain tissue is limited for a temperature of 39.2 ± 1 °C according to previous reports and guidelines (Supplementary Note 2 and Supplementary Table 4). We have also independently confirmed minimal thermal damage via immunostaining of brain slices in the presence of MINDS under our stimulation protocols (Supplementary Fig. 18). Taken together, we have demonstrated neural stimulation of deep-brain regions located ca. 6 mm underneath the scalp with distant NIR-II light, which eliminates the needs for any brain implants or optical fibres, while permitting mouse behavioural study in a large-size arena such as the Y-maze (Supplementary Table 1).

Discussion

Here, we report a NIR-II light-based neuromodulation approach for the experimental manipulation of neural activity in a depth range from 1 mm to 6 mm underneath the scalp of freely behaving animals. We paired the neuron-specific ectopic expression of heat-sensitive TRPV1 ion channels, which were recently reported to endow NIR vision to rodent and human retinas[29], with NIR-II absorbing polymeric nanoparticles (MINDS) as light sensitizers to achieve remote control of neuronal activity *in vivo*. In coupling these two systems, we demonstrated controlled activation of TRPV1 channels in neurons, resulting in significant behavioural and electrophysiological changes. Many optogenetic and chemogenetic systems now exist for controlling neuronal activity, each with its particular advantages and disadvantages. The NIR-II neuromodulation method we report here provides an alternative method in the optical neuromodulation toolbox with some salient advantages over existing approaches.

Utility of NIR-II neuromodulation for *in vivo* applications.

NIR-II optogenetic neuromodulation sits in a "sweet spot" between conventional optogenetics and chemogenetics.

Conventional optogenetics uses visible light to activate a wide range of opsins, with the longest wavelengths reported for one-photon activation of red-shifted opsins at 635 nm[14,15]. Due to the strong scattering and absorption of visible photons (400–750 nm) in the brain, skull, and scalp[9,31], a chronic brain implant of an optical fiber[45] or a microLED[13] is usually required to deliver light to deep-brain regions, whereas transcranial red-light delivery can penetrate to a depth of 7 mm by mounting the optical fibre above the exposed skull of head-tethered animals[14,15,18,19]. In the latter example, optical fibres need to be fixed on the exposed skull to meet the high incident power requirement of 400 mW mm^{-2} due to the strong attenuation of 635-nm light in the brain. In contrast, the brain effective attenuation coefficient at 1064 nm is less than half of that at 635 nm (Supplementary Fig. 1,2), thus enabling neuromodulation of untethered animals with an incident power density of 10 mW mm^{-2} from a distant light source placed >50 cm above the mouse head. This low power requirement frees the animals from the tethering of an optical fibre, since even widefield, spread illumination can easily reach the required level of power density. Additionally, two-photon activation of opsins enables deeper brain penetration, yet this technique requires a coherent, focused laser beam in head-fixed animals[17]. Moreover, although 980-nm NIR irradiation has been used for deep-brain optogenetics assisted by upconversion micro/nanoparticles, 980-nm light is near one of the major absorption bands of water abundant in the brain tissue[9], thus leading to non-specific tissue heating and a limited penetration depth. Specifically, fibreless optogenetics enabled neuromodulation up to a depth of 2~3 mm in the mouse brain via a diffuse, high-power NIR laser ~ 20 cm above the subject to excite upconversion microparticles[22]. Additionally, deep-brain optogenetics based on upconversion nanoantennas required a tethered fibre interface for efficient light delivery due to the limited penetration depth[21]. In these examples, the absorption wavelengths and energy conversion efficiencies of upconversion nanoparticles are limited by the intrinsic

electronic structures of lanthanide ions[49], thereby prohibiting using the most brain-penetrant wavelengths to efficiently modulate neural activity in the deep brain.

Despite recent advances, two challenges remain for conventional optogenetics: first, the chronic brain implants result in the permanent occupation of the neural tissue and a chronic immune response characterized as gliosis at the implant/tissue interface[11,13]. Second, head fixing and tethering restricts the study of more complex, ethologically relevant behavioural paradigms. For example, head tethering to an optical fibre confounds behavioural experiments due to the restriction of the animals' natural behaviours and limits the study of socially interacting animals (Supplementary Table 1). Specifically, for behavioural studies that involve animals in a confined space, such as the tube test for studying social hierarchy[12] and the acute stress test in a restrainer[50], it is challenging to use a fibre-tethered interface. A fibre-tethered interface is also incompatible with social behavioural studies that involve multiple mice in the same cage (e.g., the IntelliCage) due to potential tangling and biting of the fibers[51]. A similar head-fixed setup is required for sonogenetic[52] and sono-optogenetic[23] neuromodulation. In contrast, NIR-II neuromodulation enables free motion and interaction of the subjects via an implant-free and tether-free stimulation interface, since distant 1064-nm light sources can target each animal from ~1 m above while still meeting the incident power requirement due to deep-brain penetration. In summary, our approach demonstrates a minimal chronic immune response due to the elimination of brain implants (Supplementary Fig. 8) and allows natural behavioural study of freely moving and potentially socially interacting animals in future studies due to the removal of head-tethered optical fibres (Fig. 3,5)[12].

Additionally, our approach enables much shorter onset and offset response times than chemogenetic neuromodulation. Similar to our approach, chemogenetics does not require any brain implants or head tethering, but is limited by the relatively coarse temporal resolution of neuronal manipulation[26,27]. In this work, we report an onset time of ~5 s and an offset time of ~11 s for *in vivo* NIR-II neuromodulation under a safe laser power density of 8 mW mm^{-2} (Fig. 3). These response times are remarkably shorter than those reported for chemogenetics (~min onset and ~h offset)[26,27]. The latency of our approach does not rely on the slow pharmacokinetics of any molecular actuators but is instead determined by the rate of heating and cooling of NIR-II sensitizers, MINDS, in the brain tissue. The strong absorption of MINDS at the 1064-nm wavelength (Fig. 1e), along with the 2.3-fold increase in TRPV1 channel conductance from 37 °C to 39 °C (Supplementary Note 1)[30], contribute to the seconds-level latency times of neural activation and inactivation. These seconds-level latency times of NIR-II neuromodulation agree with temperature dynamics in the brain (Supplementary Fig. 12b) and represent a major advantage over chemogenetics.

Compared to magnetothermal neuromodulation[24,25], our approach allows for manipulating the behaviours of freely moving animals with an unlimited arena size (Supplementary Table 3). This advantage is due to negligible attenuation of NIR-II light in free space vs. the $1/r$ decay of the alternating magnetic field with distance from the coil, according to the Biot-Savart law. Although we only demonstrated an arena size of up to 60 cm for NIR-II photothermal neuromodulation, we envisage this method to be applicable in an arena with unlimited sizes since 1064-nm light experiences virtually no decay in air. In addition, the

photothermal conversion efficiency of MINDS (3.1×10^4 W g^{-1} at 8 mW mm^{-2}) is higher than the magnetothermal conversion efficiency of superparamagnetic nanoparticles driven by alternating magnetic field (ca. 200 W g^{-1} at 7.5 kA m^{-1} and 1 MHz)[24]. As a result, NIR-II light can be applied to an unlimited size of the behavioural apparatuses, whereas a spatially confined magnetic coil is required to produce a sufficiently strong magnetic field. Another consequence of the higher heating efficiency of our approach is the shorter onset response time of NIR-II photothermal neuromodulation (~5 s) than that of magnetothermal stimulation (~22 s) in mouse behavioural studies[24].

Compared to other photothermal neural stimulation approaches[5,39,53–55], our NIR-II photothermal method has the following advantages (Supplementary Table 3). First, our approach is the only photothermal neural modulation method that has been demonstrated in free-moving animals, owing to the tissue attenuation minimum at 1064 nm (Supplementary Fig. 1) and the unique optical properties of MINDS (Fig. 1e). Most of the existing photothermal neural stimulation reports were limited to *in vitro* due to the use of short-wavelength light in the visible and NIR-I, which exhibit severe absorption and scattering from the brain tissue[5,6,39,53–55]. Much longer infrared wavelengths of 1889 nm and 1869 nm have also been reported to stimulate cells via photothermally induced membrane capacitive current[40]; however, water absorption (Supplementary Fig. 1) becomes a major challenge when applying these wavelengths *in vivo*. Our rational choice of 1064-nm light, in contrast, represents the longest wavelength used for *in vivo* neural modulation and offers the greatest brain tissue penetration in the entire visible to NIR spectrum (Supplementary Fig. 1,2). Specifically, 1064-nm light penetrates >10x deeper than 532-nm light, the latter of which was only demonstrated for neuromodulation in cultured cells[5,39]. Second, our approach uses the lowest power density for both *in vitro* and *in vivo* studies, with the power density for *in vivo* study within the reported safe exposure limit of 10 mW mm^{-2} at 1064 nm[41]. This low power requirement is due to the efficient sensitization of MINDS, which demonstrates one of the highest photothermal conversion efficiencies in the NIR-II spectrum (Supplementary Table 2). The low power density also allowed fine control of the brain temperature without causing thermal damage (Supplementary Fig. 18, Supplementary Table 4, and Supplementary Note 2). Third, selective transduction of TRPV1 enables cell-type specific modulation of neural activity (Fig. 4,6), in contrast to non-selective photothermal neuromodulation based on optocapacitive mechanisms[5,6,39,40]. Using multiple assays including animal behaviours, *in vitro* calcium imaging, *in vivo* extracellular recordings, and immunohistological imaging, we have proved the ability of NIR-II neuromodulation to target specific cell types without interference from undesired non-specific activation. Although only neuron activation is demonstrated in this work, we envisage that specific TRPV1 expression in GABAergic neurons should enable effective inactivation of pyramidal neurons with NIR-II light[56].

Potential limitations of *in vivo* NIR-II neuromodulation.

While the NIR-II neuromodulation approach reported here overcomes some of the previous challenges as discussed above, we acknowledge potential limitations of this system.

The primary disadvantage of the *in vivo* NIR-II neuromodulation method is the slow response time (~s), which is still much longer than most optogenetics approaches to activate excitatory opsins (~ms). These relatively slow kinetics of neural activation makes this approach unfavourable for certain neurobiological events that happen on the order of milliseconds[1]. However, some behavioural experiments and many neurological diseases occur on a time scale of days to even years[57], while neuromodulation techniques with much longer latency time of minutes (e.g. chemogenetics) have also achieved widespread utility for probing neural circuits in animal models[27]. Thus, we believe that with the advantage of a tether-free brain interface, our approach is particularly suitable for behavioural studies of socially interacting animals, such as in the IntelliCage[51], which remain to be explored in future studies. Specifically, we envision that our method at its current stage can be readily applied to stimulate an animal when it interacts with multiple other animals by remotely irradiating NIR-II light. For future development of this approach, the tracking stability and efficiency can be improved with a real-time computer-vision assisted feedback loop to control the irradiation angle of the laser collimator[58].

Another disadvantage of the *in vivo* NIR-II neuromodulation method is the heating of brain tissue, which has been reported to complicate the interpretation of the behavioural results due to the suppression of neural activity[44]. Nonetheless, by comparing the results of electrophysiological, behavioural, and immunohistological studies between the TRPV1+ and TRPV1− animal groups (Fig. 3h, 4, 5e, 6 and Supplementary Fig. 11), we have not found any statistically significant activation or suppression of neural activity solely due to heating of brain tissue to ~39 °C. Besides, heating of the brain tissue to 39 °C, which was sufficient to significantly increase the conductance of TRPV1 channels (Supplementary Note 1)[30], does not cause thermal damage to the brain tissue (Supplementary Fig. 18, Supplementary Table 4, and Supplementary Note 2).

Although we have achieved noninvasive control over specific neural cell types during the behavioural experiments, TRPV1 transgene delivery and MINDS sensitization still involve invasive intracranial injections and may cause a similar level of acute invasiveness as other neural modulation techniques[13,21,25]. Nonetheless, we anticipate that this invasive procedure can be mitigated by systemic delivery of TRPV1 using AAV-PHP.eB virus[59] or creating a transgenic mouse line with specific expression of TRPV1 in neurons[60]Furthermore, the relatively small sizes of MINDS and their low amount needed for elevating c-Fos expression in the M2 suggest the possibility of less invasive delivery of MINDS through ultrasound-mediated blood brain barrier (BBB) openings[61], which remains to be explored in the future work. Additionally, we have demonstrated that MINDS remain functionally stable *in vivo* for at least 2 weeks after delivery into the brain with only a slight decrease in heating capability under NIR-II light, probably due to gradual diffusion from the injection site over time (Supplementary Fig. 17). More comprehensive studies are needed in the future to evaluate the functional lifetime and clearance pathways of MINDS from the brain for chronic *in vivo* NIR-II neuromodulation.

To conclude, in this study we describe the validation and utility of deep-brain neuromodulation with distant NIR-II illumination, which penetrates deep into the brain through the scalp and skull to selectively activate MINDS-sensitized TRPV1 channels

in neurons. The utility of our method sits between optogenetics and chemogenetics: it eliminates the chronic brain implants and fibre tethering required for optogenetics and features a more precise temporal control of activation and inactivation than chemogenetics. Therefore, the NIR-II neuromodulation approach reported here allows timely behavioural modulation of freely moving subjects with minimal chronic gliosis in the neural tissue and no interference to natural animal behaviours. With complete elimination of any brain implant and head tethering, our approach could afford wide applications in dissecting the complex neural circuits of normally behaving animals in a naturally interacting environment such as the IntelliCage in the future[51]. When combined with a red-shifted bioluminescent reporter[62], our method offers an alternative approach of optical neuromodulation with an orthogonal wavelength and may realize an all-optical bidirectional neural interface through the scalp in behaving animals.

Methods

Synthesis of *m*acromolecular *i*nfrared *n*anotransducers for *d*eep-brain *s*timulation (MINDS).

Chemicals were purchased from Sigma-Aldrich unless otherwise claimed. Benzobisthiadiazole (CS10361) was purchased from Luminescence Technology Corp (Lumtec, New Taipei City, Taiwan). Briefly, 4,7-bis(5-bromo-4-(2-octyldodecyl)thiophen-2-yl)bisbenzothiadiazole (CS10361, 25 mg, 0.023 mmol), *trans*-1,2-bis(tributylstannyl)ethene (16 μL, 0.03 mmol), tris(dibenzylideneacetone)dipalladium(0) ($Pd_2(dba)_3$, 0.6 mg, 0.00066 mmol), and tri(*o*-tolyl)phosphine (1.8 mg, 0.006 mmol) were weighed and transferred to a 50 mL Schlenk flask followed by dissolution in chlorobenzene (8 mL). After 3 cycles of freeze-pump-thaw degassing, the abovementioned mixture was heated at 100 °C in oil bath under the protection of nitrogen atmosphere to perform Stille polycondensation (Supplementary Fig. 3). After reaction for 100 minutes, the obtained mixture was added dropwise to cold methanol under vigorous stirring, followed by centrifugation at 9000 rpm for 10 minutes at 0 °C to collect dark precipitates[63]. The obtained precipitates were then washed with cold methanol for 3 times and dried under vacuum pump to afford purified poly(benzobisthiadiazole-*alt*-vinylene) (pBBTV) powder. ^{1}H NMR for pBBTV ($CDCl_3$, σ ppm): 7.6–7.0 (s, 4H), 2.6–2.1 (m, 4H), 1.9–1.8 (m, 2H) (Supplementary Fig. 4).

To obtain MINDS, the as-prepared pBBTV (0.1 mg) was weighed and co-dissolved with poly(lactide-co-glycolide)-*b*-poly(ethylene glycol) (PLGA-PEG, PLGA M_n 4500, PEG M_n 2000) (4 mg) in tetrahydrofuran (THF, 2 mL). Subsequently, the mixed solution was quickly injected into deionized water (10 mL) under vigorous ultrasonication to afford homogenous suspension, followed by evaporation of THF under a gentle N_2 flow for 40 minutes. The remaining aqueous solution was then sufficiently sonicated and filtered through polyvinylidene fluoride syringe driven filter (220 nm, Millipore, Burlington MA) to remove impurities and precipitates. To afford stock solution, the filtered MINDS solution was concentrated via ultracentrifugation at 3500 rpm at 4 °C for 25 minutes (Amicon® Ultra-15 Centrifugal Filters, Molecular weight cut-off 50 kDa, Merck KGaA, Darmstadt, Germany). Aliquots of stock solution were subsequently diluted with buffer solution to designated concentrations.

Transmission electron microscopy (TEM) imaging of MINDS.

One drop (7 μL) of homogenous MINDS solution (15 μg mL^{-1}) was deposited on a formvar/carbon film coated copper grid (Inlab Supplies Pte Ltd, Singapore) and dried in a desiccator for at least 48 h. Afterwards, TEM images of MINDS were captured on a JEOL JEM 1400 transmission microscope (JEOL USA, Inc., Peabody, MA).

Dynamic light scattering (DLS) of MINDS.

Aliquot of the abovementioned MINDS solution was diluted with 1× phosphate buffered saline (PBS, pH 7.4) to a final concentration of 5 μg mL^{-1}. Then, the hydrodynamic diameter of diluted MINDS was measured by DLS on a Malvern Nano-ZS Particle Sizer (Malvern Panalytical Ltd, Malvern, UK).

UV-Vis-NIR absorption spectroscopy of MINDS.

UV-Vis-NIR absorption spectrum of MINDS solution was measured by a Cary 6000i spectrophotometer (Agilent, Santa Clara, CA) with a total path length of 1 mm, background-corrected for contribution from water. The measured range was 300–1800 nm.

Determination of photothermal conversion efficiency.

The photothermal conversion efficiency of MINDS was calculated following reported methods in the literature[64,65]. In brief, an aqueous solution of MINDS dispersed in 2 mL PBS (optical density at 1064 nm = 1) or a blank PBS solution without MINDS (2 mL) was placed in 3.5-mL quartz cuvette (Sangon Biotech, Shanghai, China) and illuminated by a 1064-nm laser (Shanghai Connet Fiber Optics Co., Ltd., Shanghai, China) at a power density of 10 mW mm^{-2}. The average temperature of the solution was monitored by a dual input J/K type thermometer (TM300, Extech Instruments, Waltham, MA) continuously and plotted as a function of time during both the heating and cooling phases. Considering the MINDS solution in the vial as the system to be studied, energy conservation of the system during the heating phase yields

$$\sum_i m_i C_{p,i} \frac{dT}{dt} = \dot{Q}_{MINDS} + \dot{Q}_{water} + \dot{Q}_{vial} - \dot{Q}_{loss}$$

where m_i and $C_{p,i}$ represent the mass and specific heat capacity, respectively, of all components in the system including the MINDS, water and the vial, T is the temperature of the solution, $\dot{Q}_{MINDS}, \dot{Q}_{water}$ and $\dot{Q}_{vial}$ are the photothermal energy input of the MINDS, water and the vial per unit time, respectively, and $\dot{Q}_{loss}$ is the energy loss from the system per unit time due to heat transfer from the system to the surrounding environment. $\dot{Q}_{MINDS}$ can be expressed as

$$\dot{Q}_{MINDS} = I(1 - 10^{-Abs})\eta$$

where I is the power of the 1064-nm laser impinging on the sample, Abs is the absorbance of the MINDS at 1064 nm, and η is the photothermal conversion efficiency. On the other hand, the energy loss from the system to environment per unit time due to heat transfer is given by

$$\dot{Q}_{loss} = hA(T - T_{env})$$

where h is the heat transfer coefficient, A is the surface area for heat transfer, and T_{env} is the temperature of the surrounding environment. When the heating curve reaches plateau, $\frac{dT}{dt} = 0$, thus

$$\dot{Q}_{MINDS} + \dot{Q}_{water} + \dot{Q}_{vial} = \dot{Q}_{loss}$$

Plugging in the expression of $\dot{Q}_{MINDS}$ and $\dot{Q}_{loss}$ yields

$$I\left(1 - 10^{-Abs}\right)\eta + \dot{Q}_{water} + \dot{Q}_{vial} = hA\left(T_{max} - T_{env}\right)$$

Therefore

$$\eta = \frac{hA(T_{max} - T_{env}) - \left(\dot{Q}_{water} + \dot{Q}_{vial}\right)}{I\left(1 - 10^{-Abs}\right)}$$

where T_{max} and T_{env} were obtained from the heating curve of the MINDS solution, I was measured with a thermal power meter (S405C, Thorlabs Inc., Newton, NJ), Abs was measured by a UV-Vis-NIR absorption spectrometer (Agilent, Santa Clara, CA).

The same heating curve was also obtained for the blank solution without MINDS, which reached a maximum temperature of T'_{max} under the same laser heating conditions. At equilibrium for the blank solution, we have

$$\dot{Q}_{water} + \dot{Q}_{vial} = \dot{Q}_{loss} = hA\left(T'_{max} - T_{env}\right)$$

Plugging the updated expression of $\dot{Q}_{water} + \dot{Q}_{vial}$ in the equation for η yields

$$\eta = \frac{hA(T_{max} - T_{env}) - hA(T'_{max} - T_{env})}{I\left(1 - 10^{-Abs}\right)} = \frac{hA(T_{max} - T'_{max})}{I\left(1 - 10^{-Abs}\right)}$$

Therefore, to obtain the photothermal conversion efficiency η, the only unknown variables in this equation are h and A. In order to measure h and A, consider the cooling phase when the system receives no energy input from the environment, thus $\dot{Q}_{MINDS} = \dot{Q}_{water} = \dot{Q}_{vial} = 0$:

$$\sum_i m_i C_{p,i} \frac{dT}{dt} = -\dot{Q}_{loss} = -hA\left(T - T_{env}\right)$$

$$\frac{\sum_i m_i C_{p,i}}{hA} \frac{dT}{T - T_{env}} = -dt$$

Integrating both sides yield

$$\frac{\sum_i m_i C_{p,i}}{hA} ln\left(\frac{T - T_{env}}{T_{max} - T_{env}}\right) = -t$$

Therefore, by plotting $ln\left(\frac{T - T_{env}}{T_{max} - T_{env}}\right)$ as a function of time t during the cooling phase, one obtains the value hA from the slope of linear fitting. Note that $\sum_i m_i C_{p,i}$ was calculated to be 12.928 J/K based on the mass and the specific heat capacity of quartz container and water.

Preparation of MINDS-Fluor.

To obtain MINDS-Fluor (MINDS labelled with a green fluorophore), a fluorescence dye 1-chloro-9,10-bis(phenylethynyl)anthracene (0.025 mg) was co-dissolved with pBBTV (0.1 mg) and PEG-PLGA (4 mg) in THF (2 mL), followed by rapid injection into deionized water (8 mL) during vigorous sonication. Thereafter, THF in the aqueous solution was removed by a gentle air flow for 40 minutes. The nanoparticle suspension was filtered through polyvinylidene fluoride syringe driven filter (220 nm, Millipore) and concentrated via ultracentrifugation at 3500 rpm at 4 °C for 25 minutes to obtain stock solutions. Aliquots of stock solution were diluted with buffer solution to designated concentrations before use.

Calculation of brain effective attenuation coefficient.

The brain effective attenuation coefficient (μ_e) was calculated as[66,67]:

$$\mu_{eff} = \sqrt{3\mu_a \cdot (\mu_a + \mu_s')}$$

where μ_a is the brain's absorption coefficient and μ_s' is the brain's reduced scattering coefficient. μ_s' was calculated based on the brain scattering coefficient (μ_s) as:

$$\mu_s' = (1 - g) \cdot \mu_s$$

where g is the anisotropy factor. The values for μ_s and g were taken from previous reports[68].

The brain's absorption coefficient was calculated using the absorption coefficients of water[69], lipid[69], oxyhemoglobin and deoxyhemoglobin[70], and reduced and oxidized cytochrome c oxidase[71] weighted by their compositions or concentrations in the brain tissue[72].

Monte Carlo simulation.

Two-dimensional Monte Carlo simulations were performed using MATLAB following a similar procedure as previously reported[73]. The simulation sent photon packets with initial energy E into the scalp at normal incidence. Packets were uniformly distributed within 1 cm centred at the MINDS injection site to match the laser spot size used during experiments. A step size of 10 or 100 μm was used to bin the 10 mm deep × 25 mm wide simulation space. Between scattering events, photon packets travelled a distance of $d = -\ln(RAND)/\mu_s$. Scattering was considered to be anisotropic, and the scattering angle θ was within a range determined by the anisotropy factor g as $g = <\cos\theta>$. The distribution of scattering angles was taken from reference[74]. For each travelled distance between two consecutive scattering events, the packet energy decreased by a factor of $exp(-\mu_a \cdot distance)$. The lost energy was assigned to each traversed pixel (determined by binning) as the absorbed energy. When crossing an interface between scalp, skull, or brain tissue, the refraction of the packet was calculated using the refractive index n of different mediums according to Snell's Law. The optical properties of scalp[75–77] and skull[78–80] and brain tissue[68,81] were taken from previous reports.

Simulation of temperature dynamics.

The temperature dynamics in the brain tissue was simulated by solving the Pennes bioheat equation:

$$\frac{dT}{dt} = \frac{k_t}{\rho_t \cdot C_{v,t}} \cdot \nabla^2 T + \frac{P_i}{\rho_t \cdot C_{v,t}} - \frac{\rho_b \cdot C_{v,b} \cdot f_b \cdot (T - T_b)}{C_{v,t}}$$

where k is the thermal conductivity, ρ is the density, C_v is the specific heat, T is the temperature, and P_i is the power input per unit volume induced by NIR-II illumination, obtained from Monte Carlo simulation. The subscript 't' and 'b' represents tissue and blood, respectively. The three terms on the right-hand side of the equation represent the temperature change induced by thermal diffusion, NIR-II illumination and blood perfusion, respectively. The physical parameters used for this simulation are summarized in Supplementary Table 5. To set boundary conditions, we empirically determined a cooling rate from the scalp to the air above such that the top of the scalp was steady at 36.5 °C (matching measurements of mouse scalp temperature using a thermal camera) when the system was solved with the Pennes bioheat equation in the absence of NIR-II illumination. The resulting temperature distribution (dependent on depth in the tissue) was used as the initial conditions throughout the domain and was also maintained on the left and right edges of the domain as boundary conditions throughout the duration of the simulation. The bottom of the domain was held at 37 °C as the core body temperature throughout the duration of the simulation.

Viral vector construction.

Viral vectors used in this work include: pAAV-CMV-TRPV1-mCherry plasmid was constructed by Vector Biolabs (Malvern, PA), AAV5-eSyn-TRPV1-p2A-mCherry virus, and AAV5-EF1a-DIO-TRPV1 virus were constructed and packaged by Vector Biolabs (Malvern, PA). For transduction in the secondary motor cortex (M2) with AAV5-eSyn-TRPV1-p2A-

mCherry, it has been reported that the synapsin (Syn) promoter is neuron-specific with little glial expression[82].

Cytotoxicity test of MINDS.

Cytotoxicity of MINDS was tested on rat hippocampal primary neurons isolated from Sprague Dawley rat embryos and placed in a 96-well plate. Neuron culture was maintained in Neurobasal-A medium (Gibco) supplemented with 4.5 g L^{-1} glucose, B-27 (Gibco) and 0.5% fetal bovine serum (FBS; Gibco). 2 weeks after isolation, the neurons were incubated with 200 μL MINDS solution of different concentrations (0 – 3.6 mg mL^{-1}) in neuron culture medium for 24 h, and an additional group of neurons were incubated with 5% DMSO as the positive control. After the incubation, the supernatant was removed, and cells were gently washed with fresh $1\times$ PBS. Colorimetric MTT (3-(4,5-dimethylthiazol-2-yl)-2,5-diphenyltetrazolium bromide) assays (Invitrogen, Carlsbad, CA) were performed according to the manufacturer's instruction. Absorbance at 590 nm was subsequently recorded on a SPECTRAFluor Plus microplate reader (Tecan Group Ltd., Männedorf, Switzerland). Cell viability was calculated as the ratio of absorbance from MINDS-treated or DMSO-treated cells to that of negative control cells incubated in blank medium.

Cell culture and transfection.

Human embryonic kidney (HEK) 293T cells were purchased from MilliporeSigma (Burlington, MA). Cell culture was maintained in Dulbecco's modified Eagle's medium with 4.5g L^{-1} glucose (DMEM; Gibco) supplemented with 10% FBS (Gibco). HEK293T cells were transfected with 7.5 μL of lipofectamine ® 3000 (Invitrogen, Carlsbad, CA) with 2500 ng of total DNA of the pAAV-CMV-TRPV1-mCherry plasmid in Opti-MEM medium (Gibco), and used for calcium imaging during near-infrared-II (NIR-II) photothermal stimulation 3–5 days after transfection.

In vitro NIR-II stimulation and calcium imaging.

HEK293T cells were seeded into Confocal Dishes (VWR, Radnor, PA) and allowed to adhere for 24 h in a humidified atmosphere containing 5% CO_2 and 95% air at 37 °C. The cells were treated with MINDS at a final concentration of 70 μg mL^{-1} for 24 h in culture medium. Cells were washed 2 times with $1\times$ PBS, stained in Hank's Buffer with 20 mM Hepes solution (HHBS; AAT Bioquest, Sunnyvale, CA; containing 140 mg L^{-1} $CaCl_2$) containing the Cal-520® AM fluorescent indicator (AAT Bioquest, Sunnyvale, CA) prior to live-cell imaging. LSM 780 confocal microscope (Carl Zeiss Microscopy GmbH, Jena, Germany) was used for calcium imaging with an excitation wavelength of 488 nm and an emission window of 500–520 nm for image formation. For NIR-II photothermal stimulation, a built-in 1040 nm laser was focused to a spot size of 250 μm and a power density of 400 mW mm^{-2}. The average power density of 1040-nm laser used for photothermal stimulation was significantly lower than previously reported power density using 780 nm (8×10^3 mW mm^{-2}) and 808 nm (10^5 mW mm^{-2}) laser[53,64], owing to the much higher photothermal conversion efficiency of 71% measured for MINDS. Real-time calcium imaging was timed with NIR-II photothermal stimulation from the 1040-nm laser, which was turned on and off on selected regions of the cell culture. Average fluorescence intensity of Cal-520® AM

indicator was analysed using custom-written MATLAB code with the built-in *roipolyarray* function[83].

Vertebrate animal subjects.

Adult (20–30 g) C57BL/6J mice (male, 6 weeks old, Charles River Laboratories, Wilmington, MA) and TH-Cre transgenic mice (male, 6 weeks old, Jackson Laboratory, Bar Harbor, ME) were the vertebrate animal subjects used in this study. All procedures performed on the mice were approved by Stanford University's Administrative Panel on Laboratory Animal Care (APLAC). The animal care and use programs at Stanford University meet the requirements of all federal and state regulations governing the humane care and use of laboratory animals, including the USDA Animal Welfare Act, and PHS Policy on Humane Care and Use of Laboratory Animals. The laboratory animal care program at Stanford is accredited by the Association for the Assessment and Accreditation of Laboratory Animal Care (AAALAC International). Animals were group-housed on a 12 h: 12 h light: dark cycle (temperature: 20–25 °C, humidity: 50–65 %) in the Stanford University's Veterinary Service Center (VSC) and fed with food and water *ad libitum* as appropriate.

In vivo stereotaxic injection of virus.

In vivo injection of virus into the brains of live mice was performed using a controlled stereotaxic injection method[84]. First, all metal tools in direct contact with the surgical subject were autoclaved for 1 h before use, and all plastic tools in direct contact with the surgical subjects were sterilized with 70% ethanol and rinsed with sterile DI water and sterile 1× PBS before use. Viral vectors were dispersed in sterile 1× PBS with 5% glycerol before injection. Mice were anaesthetized by intraperitoneal injection of a mixture of 80 mg kg^{-1} of ketamine (KetaVed®, Vedco, Inc., St. Joseph, MO) and 1 mg/kg dexdomitor (Dexmedesed™, Dechra Veterinary Products, Overland Park, KS). The degree of anaesthesia was verified via the toe pinch method before the surgery started. Buprenorphine SR-LAB (Zoopharm, Inc., Windsor, CO) analgesia was given subcutaneously at a dose of 1 mg kg^{-1} body weight before the surgery. To maintain the body temperature and prevent hypothermia of the surgical subject, a homeothermic blanket (Harvard Apparatus, Holliston, MA) was set to 37 °C and placed underneath the anaesthetized mouse, which was placed in the stereotaxic frame (World Precision Instruments, Inc., Sarasota, FL) equipped with two ear bars and one nose clamp that fix the mouse head in position. Vet ointment (Puralube®, Dechra Veterinary Products, Overland Park, KS) was applied on both eyes of the mouse to moisturize the eye surface throughout the surgery. Hair removal lotion (Nair®, Church & Dwight, Ewing, NJ) was used for depilation of the mouse head according to the manufacture's instruction and iodophor was applied to sterilize the depilated scalp skin. A 1-mm longitudinal incision was made with a sterile scalpel, followed by elongation of the incision by surgical scissors to expose the cranial bone immediately above the targeted brain regions for injection without removing any scalp skin. The incisions were made near the distal periphery of the scalp opposite the injection site for unilateral stereotaxic injections later, thus ensuring the wound in the scalp would not block the underlying neural tissue from overhead NIR-II illumination for behavioural modulation.

The following stereotaxic coordinates were used for injection of viral vectors and MINDS:

Secondary motor cortex (M2)[3,24,45]: Anteroposterior (AP) +1.0 mm, mediolateral (ML) ±0.5 mm (+0.5 for right hemisphere and −0.5 for left hemisphere), dorsoventral (DV) −0.5 mm

Hippocampus (HIP)[85]: AP −1.5 mm, ML ±1.5 mm, DV −1.5 mm

Ventral tegmental area (VTA)[21,86]: AP −3.5 mm, ML ±0.4 mm, DV −4.2 mm

For each animal, according to the targeted brain region, a 0.5 mm diameter burr hole was drilled using a dental drill (Marathon-III) according to the AP and ML coordinates described above. 2.5 μL of AAV solution was injected into M2, HIP or VTA region of the brain using NanoJet (Chemyx, Inc., Stafford, TX) with a 33-gauge needle (Hamilton Company, Inc., Reno, NV) facing the ventrolateral side at 0.1 μL min^{-1}. AAV5-eSyn-TRPV1-p2A-mCherry virus (2.2×10^{12} GC ml^{-1}) was used for M2 or HIP transduction in C57BL/6J mice, while AAV5-EF1a-DIO-TRPV1 virus (3.6×10^{12} GC ml^{-1}) was used for VTA transduction in TH-Cre transgenic mice. After injection of viral vectors, the syringe needle was allowed to stay inside the brain for 2 min before withdrawal. The incised scalp skin was placed back to cover all exposed cranial bone, and sealed by using Vetbond tissue adhesive (3M, Maplewood, MN). Antibiotic ointment (Johnson & Johnson Consumer, Inc., Skillman, NJ) was applied copiously around the wound. The mouse was returned to the cage equipped with a 37 °C heating pad and its activity monitored every hour until fully recovered from anaesthesia (i.e., exhibiting sternal recumbency and purposeful movement). Animals with failed surgeries were discard from further experiments.

In vivo stereotaxic injection of MINDS.

In vivo injection of MINDS into the brains of live mice was performed using a controlled stereotaxic injection method similar to virus injection described above. MINDS were dispersed in sterile Hank's Buffer with 20 mM Hepes solution (HHBS; AAT Bioquest, Sunnyvale, CA; containing 140 mg L^{-1} anhydrous CaCl$_2$) before injection. Mice were anaesthetized as previously described, and scalp incision and craniotomy were performed at the corresponding coordinates for M2, HIP or VTA. 2.5 μL of MINDS solution (1.8 mg mL^{-1}) was injected into targeted brain region using NanoJet (Chemyx, Inc., Stafford, TX) with a 33-gauge needle (Hamilton Company, Inc., Reno, NV) facing the ventrolateral side at 0.1 μL min^{-1}. The same amount of HHBS instead of MINDS was injected for MINDS (−) controls. After injection of MINDS, the syringe needle was allowed to stay inside the brain for 2 min before withdrawal. The incised scalp skin was sealed as described above.

In vivo electrophysiological recordings during NIR-II neuromodulation.

Tungsten microwire electrodes (TM53A15, World Precision Instruments, Sarasota, FL) were used for *in vivo* electrophysiological recording immediately after MINDS or carrier-only injection in anaesthetized mice. A 0–80 set screw (18–8 Stainless Steel Cup Point Set Screw; outer diameter: 0.060" or 1.52 mm, groove diameter: 0.045" or 1.14 mm, length: 3/16" or 4.76 mm; McMaster-Carr Supply Company, Elmhurst, IL) was implanted into the following stereotaxic coordinates as the grounding and reference electrode: AP: −4.96 mm, ML: 3.10 mm. After implantation of the grounding screw, two tungsten electrodes were

slowly inserted into the left and right hippocampal regions (AP: −1.5 mm, ML: ± 1.5 mm, DV: −1.5 mm). After reaching the targeted regions, the electrodes were glued to the skull using METABOND® dental cement (Parkell Inc., Edgewood, NY). The tungsten probes were connected to an Intan RHD 2132 amplifier evaluation system (Intan Technologies, Los Angeles, CA), and the 0–80 set screw was used as a reference. For photothermal stimulation of the hippocampus, a 1064-nm laser was illuminated in the continuous-wave (CW) mode from a distant collimator, with a power density of 8 mW mm^{-2}. Electrophysiological recordings were acquired with a 20 kHz sampling rate and a 60 Hz notch filter. The signals were then analysed using MATLAB with a bandpass filter of 250–6000 Hz[84]. A total of 52 traces collected from 9 animals were used for statistical analysis.

NIR-II neurostimulation in the M2.

One experimental group of mice receiving both virus and MINDS injections in the M2 and three control groups of mice were used in this study. The animals were allowed to completely recover from the stereotaxic injection for 12 h and showed normal behaviours before the behavioural experiments started. It has been reported that a 12-h post-operative period is sufficient for studying neuromodulation-induced behavioural changes with minimal interference from pain or anaesthesia[24]. The hair over the scalp and neck was shaved to expose the skin, and a red or blue dot was marked on the skin between the head and the neck for tracking the animal's trajectory. For each session, one mouse was placed in a 14 cm × 15 cm arena and was allowed to explore the space in the box freely. A video camera (Rebel T6, Canon U.S.A., Inc, Melville, NY) was used to record the video (640 × 480 pixels, 25 fps) of the mouse before, during and after distant NIR-II photothermal stimulation. A fibre-coupled collimator connected to the 1064-nm laser (SOL, RPMC Laser Inc., O'Fallon, MO) illuminated a 1 cm^2 area that followed the head of the mouse in the arena. To demonstrate proof-of-concept, the illumination angle of the fibre-coupled collimator was adjusted manually to track the head of the mouse, while the tracking stability and efficiency can be further improved with a real-time computer-vision assisted feedback loop with a custom-written MATLAB code that tracks the head position of the animal (described below) to automatically control the irradiation angle of the laser collimator, as has been demonstrated in Ref. 58 can be incorporated into a closed-loop controller for automatic tracking. Precautions were taken during each session to ensure there was minimum change of shadows caused by the camera in the active area of the animal to avoid influence on the animal's behaviour. During NIR-II photothermal stimulation, the 1064-nm laser was illuminated in the continuous-wave (CW) mode in free space from the collimator, with a maximum power density of 8 mW mm^{-2}. The maximum power density was below the safe exposure limit of 10 mW mm^{-2} at 1064 nm determined by the International Commission on Non-ionizing Radiation Protection[41]. During the unilateral circling test, a thermal camera (FLIR A325sc, FLIR Systems, Inc., Wilsonville, OR) was used to monitor heating in real time by following a previously reported protocol[42] to avoid the thermal damage to the brain tissue. Specifically, a closed-loop feedback control was used to turn the laser power down to 0 mW mm^{-2} whenever the temperature rose above 39 °C and turned back up to the maximum allowed power density of 8 mW mm^{-2} when the temperature dropped below 38 °C. This closed-loop feedback control can be implemented both manually and automatically. Specifically, in an automatically controlled setup, the temperature of the scalp

from the thermal camera was acquired using the Image Acquisition Toolbox in MATLAB, and then compared with the two setpoints to control the laser output in real-time. When the temperature is lower than 38 °C, a high-level voltage of 5 V is sent as an external trigger to turn on the laser. This high-level 5 V signal is provided by the analog output from a multifunction I/O device (NI USB-6221, National Instruments, Austin, TX) controlled by MATLAB through the Data Acquisition Toolbox. Similarly, when the temperature is higher than 39 °C, the output voltage will be changed to 0 V to turn off the laser. If the temperature is between 38 and 39 °C, the voltage will remain at the prior setpoint. A typical duty cycle of the 1064-nm laser was ~ 38 % for the first pulse and ~ 18 % for the following pulses, determined during the experiments by the thermal camera.

The videos acquired from recording sessions were processed in a custom-written MATLAB code that can track both the red/blue marker on the skin and the centre of mass of the animal. Based on the trajectory of the mouse obtained thereof, and the frame rate of the video that defines the time interval between two neighbouring locations in the trajectory, the angular displacement of the animal with respect to $t = 0$ s of each session was calculated and plotted. Clockwise rotation was defined as negative angular displacement while counter-clockwise rotation was defined as positive angular displacement. Based on the data of angular displacement as a function of time in each session, angular speed of the animal was computed by dividing the number of revolutions over total length of time when the 1064-nm laser was on. Analysis of the variance (ANOVA) was performed using the built-in function 'anova1' in MATLAB to evaluate the statistical significance in angular speed when the laser was on between experimental and control groups. For the latency analysis, the onset latency time is defined as the time interval between NIR-II illumination and the start of unilateral circling, while the offset latency time is defined as the time interval between the end of NIR-II illumination and the cease of unilateral circling.

NIR-II neurostimulation in the VTA.

One experimental group of mice receiving both virus and MINDS injections in the VTA and three control groups of mice were used in this study. The animals were allowed to recover from the stereotaxic injection for 48 h before the behavioural experiments. It has been reported that a 12-h post-operative period is sufficient for the animals to recover from the surgery with normal behaviours, thus allowing for the study of neuromodulation-induced behavioural changes with minimal interference from pain or anaesthesia[24]. The hair over the scalp and neck was shaved to expose the skin. For each session, one mouse was placed in a three-compartment Y maze (Maze Engineer, Inc., Cambridge, MA). Each arm of the Y Maze was 35 cm by 5 cm, connected by an equilateral triangle with 5 cm side in the centre, resulting in a total area of 536 cm^2 for the Y maze. At the end of each arm, a unique context (white, horizontal black stripes, or vertical black stripes) was outfitted to facilitate the formation of contextual visual memory (Supplementary Fig. 13)[13].

One complete set of training and probe trials comprises five days: On Day 1, the animal was allowed to explore the space in the Y maze freely for 30 min without any NIR-II illumination. On Day 2 to 4 for training trials, the 1064-nm laser was directed via a fibre collimator to illuminate a 1 cm^2 area that followed the head of the mouse whenever its

head entered a 25 cm^2 area at the end of one of the three arms. Similar to the behavioural experiments in the M2, the illumination angle of the fibre-coupled collimator was adjusted manually to track the head of the mouse, while the tracking stability and efficiency can be further improved with a real-time computer-vision assisted feedback loop with a custom-written MATLAB code that tracks the head position of the animal (described below) to automatically control the irradiation angle of the laser collimator, as has been demonstrated in Ref. 58. The laser was modulated at 20 Hz with peak power density of 33 mW mm^{-2} in the illuminated area and a 30% duty cycle, resulting in an average power density of 10 mW mm^{-2}, within the safe exposure limit at 1064 nm determined by the International Commission on Non-ionizing Radiation Protection[41]. Similar to the unilateral circling test described above, a thermal camera was used to monitor the temperature on the scalp of the animal during the conditioning with feedback control of the laser output to avoid thermal damage to the brain tissue. The same temperature setpoints, hardware, and software interfaces as in the unilateral circling test were used for NIR-II neuromodulation in the VTA. A typical duty cycle of the 1064-nm laser was 52 % for the first pulse and 24 % for the following pulses, determined during the experiments by the thermal camera. The animal was allowed to freely explore all three arms, including the arm with 1064-nm laser illumination for a total of 30 min on each day. On Day 5 for probe trial, the animal was allowed to explore the space in the Y maze freely for 30 min without any NIR-II illumination (Supplementary Fig. 13). During each session, a video camera (VIXIA HF W11, Canon U.S.A., Inc, Melville, NY) was used to record the video (1920 × 1080 pixels, 30 fps) of the mouse. Precautions were taken during each session to ensure there was minimum change of shadows in the active area of the animal to avoid influence on the animal's behaviour.

The videos acquired from the probe trial sessions were processed in a custom-written MATLAB code that can track both the red/blue marker on the skin and the centre of mass of the animal. Based on the trajectory of the mouse obtained thereof, and the frame rate of the video, the amount of time that the animal spent in each location of the Y maze during the probe trial was plotted in a heat map for visualization of place preference. Preference score was defined as the ratio of time the mouse spent in the NIR-II illuminated arm terminal during post-test vs. pre-test trial. Analysis of the variance (ANOVA) was performed using the built-in function 'anova1' in MATLAB to evaluate the statistical significance in preference between experimental and control groups. The preference score is defined as the ratio of total time each mouse spent in the NIR-II light illuminated arm terminal during post-test vs. pre-test trials. The normalized time in the active region is defined as the ratio of the time spent in the NIR-II light illuminated arm terminal to the average time spent in the equivalent regions of the other two control arm terminals for each mouse. The normalized preference score is defined as the ratio of the normalized time in the active region in post-test trials to that in pre-test trials.

Histology.

C57BL/6J mice were anaesthetized and transcardially perfused with 1× PBS followed by 4% paraformaldehyde (PFA) in PBS. For the evaluation of the chronic immune response (Supplementary Fig. 8), transcardial perfusion was performed at 1 week and 3 weeks after the animals received MINDS or carrier injection. For the evaluation of thermal damage in

the brain (Supplementary Fig. 18), transcardial perfusion was performed at 1 week after the animals received NIR-II illumination[25]. For imaging c-Fos in the M2 and VTA (Fig. 4,6), transcardial perfusion was performed at 90 min after the animals of different experimental and control groups received NIR-II illumination. For the evaluation of *in vivo* distribution and cellular uptake of MINDS (Supplementary Fig. 15,16), transcardial perfusion was performed 72 hours after the MINDS injection. Brains were dissected, post-fixed for 24 h at 4 °C in 4% PFA and then equilibrated in 30% sucrose at 4 °C for cryoprotection. 20 μm-thick horizontal sections were collected on a cryostat (Leica CM 3050S, Leica Biosystems Inc., Buffalo Grove, IL). The brain slices were rinsed in 1× PBS three times for 10 min each and blocked using a blocking solution consisting of 0.3% Triton X-100 and 5% goat/donkey serum (from the same species in which secondary antibody is made, Jackson ImmunoResearch Laboratories, Inc., West Grove, PA) in 1× PBS for 1 h at room temperature. If mouse was used as a host species for the primary antibody, an additional 1 h blocking using a 26 μg/ml (1:50 dilution) solution of AffiniPure Fab Fragment Goat Anti-Mouse IgG (115–007-003, Jackson ImmunoResearch Laboratories, Inc., West Grove, PA) was performed. Slices were then incubated with the primary antibodies (Supplementary Table 6) containing 0.3% Triton X-100 and 5% goat/donkey serum overnight at 4 °C. After incubation, slices were rinsed in 1× PBS with 0.05% Triton X-100 three times for 10 min each, before they were incubated with the secondary antibodies (Supplementary Table 6) containing 0.1% Triton X-100 and 5% goat/donkey serum for 1 h at room temperature. Slices were then rinsed in 1× PBS three times for 10 min each before they were mounted on glass slides with coverslips using ProLong Gold Antifade Mountant (Invitrogen, Carlsbad, CA). The slides remained in the dark at room temperature for at least 24 h before microscopic imaging. Confocal fluorescence images were acquired on a Zeiss LSM 780 confocal microscope. The confocal imaging parameters were set using the "Smart Setup" function on the ZEN Blue software and were kept the same across the same experiments. The data was analysed using ImageJ 1.53 c.

Assessment of the chronic functional stability of MINDS *in vivo*.

2.5 μL of 1.8 mg mL^{-1} MINDS solution was injected into VTA of C57BL/6J mice as described above. The animals were sacrificed 1 day or 2 weeks after the injection, and 2-mm thick acute coronal sections containing the injected MINDS near the VTA were collected from the freshly dissected brains using a brain slicer (Braintree Scientific Inc., Braintree, MA) and immersed in Hank's balanced salt solution (HBSS) immediately afterwards to prevent dehydration until use. The coronal sections were then transferred to the top of a 10-mm petri-dish lid with the MINDS-injected side facing up. 10 mW mm^{-2} 1064-nm illumination was applied to the brain slice, and a thermal camera was used to monitor the temperature change. Also see the schematics in Supplementary Fig. 17a for more information.

Replication.

The sample size for each experiment was determined by power analysis to ensure statistical rigor for all comparisons[87]. The calcium fluorescence imaging experiments to investigate percentage of responsive cells (with and without MINDS, and with and without NIR-II illumination) have been repeated on 3 independent trials for each experimental

condition, resulting in 12 trials in total. The dynamic calcium imaging experiments to investigate the fluorescence intensity change and latency time upon NIR-II illumination have been repeated for 9 times for each experimental condition, resulting in 36 replicates in total. The assessment of chronic immune response has been repeated on 3 mice at each time points and experiment conditions, resulting in 12 mice. The assessment of thermal damage has been repeated on 3 mice with or without NIR-II illumination for both the M2 and VTA illumination protocols, resulting in 12 mice. The unilateral circling experiments to investigate widefield NIR-II modulation of motor behaviour (angular speed and latency time) have been repeated on a total of 15 animals and 37 trials. The *in vivo* electrophysiological studies have been repeated on 9 animals and 44 traces. The assessment of chronic functional stability of MINDS has been repeated on 3 mice for each time point with or without MINDS injection, resulting in a total of 9 mice. In addition, investigations of NIR-II modulation of reward circuitry and place preference have been repeated on a total of 18 independent animals. In total, experiments and analyses of 75 mice were included for replication.

Statistical analysis.

The variance in calcium fluorescence intensity (Fig. 2), angular speed (Fig. 3) place preference (Fig. 5), cell density and population percentage (Fig. 4, 6 and Supplementary Fig. 18), raw and normalized neural firing rate (Supplementary Fig. 11), *ex vivo* temperature measurements (Supplementary Fig. 17) for each cell, animal, behavioural trial or electrophysiological traces was calculated, by which the pooled standard deviation (SD) among each experimental group were determined. Comparisons between experimental groups were made using one-way analysis of variance (ANOVA) without normality assumption given its reasonable tolerance of violations to normal distribution[87]. No adjustments were made for multiple comparisons, and P values of less than 0.05 were considered statistically significant.

Reporting Summary.

Further information on research design is available in the Nature Research Reporting Summary linked to this article.

Data availability

The main data supporting the results in this study are available within the paper and its Supplementary Information. The raw and analysed datasets generated during the study are too large to be publicly shared, yet they are available for research purposes from the corresponding authors on reasonable request.

Code availability

The custom MATLAB code used in this study is available at https://github.com/XiangWu96/Wu_NBME_21_code.

Supplementary Material

Refer to Web version on PubMed Central for supplementary material.

Acknowledgements

References

1. Fenno L, Yizhar O & Deisseroth K The development and application of optogenetics. Annu. Rev. Neurosci. 34, 389–412 (2011). [PubMed: 21692661]

2. Tsai H-C et al. Phasic firing in dopaminergic neurons is sufficient for behavioral conditioning. Science 324, 1080–1084 (2009). [PubMed: 19389999]

3. Montgomery KL et al. Wirelessly powered, fully internal optogenetics for brain, spinal and peripheral circuits in mice. Nat. Methods 12, 969–974 (2015). [PubMed: 26280330]

4. Lozano AM et al. Deep brain stimulation: current challenges and future directions. Nat. Rev. Neurol. 15, 148–160 (2019). [PubMed: 30683913]

5. Carvalho-de-Souza JL et al. Photosensitivity of neurons enabled by cell-targeted gold nanoparticles. Neuron 86, 207–217 (2015). [PubMed: 25772189]

6. Jiang Y et al. Rational design of silicon structures for optically controlled multiscale biointerfaces. Nat Biomed Eng 2, 508–521 (2018). [PubMed: 30906646]

7. DiFrancesco ML et al. Neuronal firing modulation by a membrane-targeted photoswitch. Nat. Nanotechnol. 15, 296–306 (2020). [PubMed: 32015505]

8. Hong G & Lieber CM Novel electrode technologies for neural recordings. Nat. Rev. Neurosci. 20, 330–345 (2019). [PubMed: 30833706]

9. Hong G, Antaris AL & Dai H Near-infrared fluorophores for biomedical imaging. Nat. Biomed. Eng. 1, 1–22 (2017).

10. Ledesma HA et al. An atlas of nano-enabled neural interfaces. Nat. Nanotechnol. 14, 645–657 (2019). [PubMed: 31270446]

11. Salatino JW, Ludwig KA, Kozai TDY & Purcell EK Glial responses to implanted electrodes in the brain. Nat. Biomed. Eng. 1, 862–877 (2017). [PubMed: 30505625]

12. Fan Z et al. Using the tube test to measure social hierarchy in mice. Nat. Protoc. 14, 819–831 (2019). [PubMed: 30770887]

13. Kim T-I et al. Injectable, cellular-scale optoelectronics with applications for wireless optogenetics. Science 340, 211–216 (2013). [PubMed: 23580530]

14. Lin JY, Knutsen PM, Muller A, Kleinfeld D & Tsien RY ReaChR: a red-shifted variant of channelrhodopsin enables deep transcranial optogenetic excitation. Nat. Neurosci. 16, 1499–1508 (2013). [PubMed: 23995068]

15. Chuong AS et al. Noninvasive optical inhibition with a red-shifted microbial rhodopsin. Nat. Neurosci. 17, 1123–1129 (2014). [PubMed: 24997763]

16. Rajasethupathy P et al. Projections from neocortex mediate top-down control of memory retrieval. Nature 526, 653–659 (2015). [PubMed: 26436451]

17. Marshel JH et al. Cortical layer–specific critical dynamics triggering perception. Science 365, eaaw5202 (2019). [PubMed: 31320556]

18. Chen R et al. Deep brain optogenetics without intracranial surgery. Nat. Biotechnol. 39, 161–164 (2021). [PubMed: 33020604]

19. Gong X et al. An ultra-sensitive step-function opsin for minimally invasive optogenetic stimulation in mice and macaques. Neuron 107, 38–51 (2020). [PubMed: 32353253]

20. Bedbrook CN et al. Machine learning-guided channelrhodopsin engineering enables minimally invasive optogenetics. Nat. Methods 16, 1176–1184 (2019). [PubMed: 31611694]

21. Chen S et al. Near-infrared deep brain stimulation via upconversion nanoparticle-mediated optogenetics. Science 359, 679–684 (2018). [PubMed: 29439241]

22. Miyazaki T et al. Large timescale interrogation of neuronal function by fiberless optogenetics using lanthanide micro-particles. Cell Rep. 26, 1033–1043.e5 (2019). [PubMed: 30673599]

23. Wu X et al. Sono-optogenetics facilitated by a circulation-delivered rechargeable light source for minimally invasive optogenetics. Proc. Natl. Acad. Sci. USA 116, 26332–26342 (2019).

24. Munshi R et al. Magnetothermal genetic deep brain stimulation of motor behaviors in awake, freely moving mice. eLife 6, e27069 (2017). [PubMed: 28826470]

25. Chen R, Romero G, Christiansen MG, Mohr A & Anikeeva P Wireless magnetothermal deep brain stimulation. Science 347, 1477–1480 (2015). [PubMed: 25765068]

26. Alexander GM et al. Remote control of neuronal activity in transgenic mice expressing evolved G protein-coupled receptors. Neuron 63, 27–39 (2009). [PubMed: 19607790]

27. Magnus CJ et al. Ultrapotent chemogenetics for research and potential clinical applications. Science 364, eaav5282 (2019). [PubMed: 30872534]

28. Smith AM, Mancini MC & Nie S Second window for in vivo imaging. Nat. Nanotechnol. 4, 710–711 (2009). [PubMed: 19898521]

29. Nelidova D et al. Restoring light sensitivity using tunable near-infrared sensors. Science 368, 1108–1113 (2020). [PubMed: 32499439]

30. Grandl J et al. Temperature-induced opening of TRPV1 ion channel is stabilized by the pore domain. Nat. Neurosci. 13, 708–714 (2010). [PubMed: 20414199]

31. Bashkatov AN, Genina EA, Kochubey VI & Tuchin VV Optical properties of human skin, subcutaneous and mucous tissues in the wavelength range from 400 to 2000 nm. J. Phys. D: Appl. Phys. 38, 2543–2555 (2005).

32. Miao Q et al. Molecular afterglow imaging with bright, biodegradable polymer nanoparticles. Nat. Biotechnol. 35, 1102–1110 (2017). [PubMed: 29035373]

33. Gracheva EO et al. Molecular basis of infrared detection by snakes. Nature 464, 1006–1011 (2010). [PubMed: 20228791]

34. Huang H, Delikanli S, Zeng H, Ferkey DM & Pralle A Remote control of ion channels and neurons through magnetic-field heating of nanoparticles. Nat. Nanotechnol. 5, 602–606 (2010). [PubMed: 20581833]

35. Yao J, Liu B & Qin F Rapid temperature jump by infrared diode laser irradiation for patch-clamp studies. Biophys. J. 96, 3611–3619 (2009). [PubMed: 19413966]

36. Davis HC et al. Nanoscale heat transfer from magnetic nanoparticles and ferritin in an alternating magnetic field. Biophys. J. 118, 1502–1510 (2020). [PubMed: 32061270]

37. Moiseenkova-Bell VY, Stanciu LA, Serysheva II, Tobe BJ & Wensel TG Structure of TRPV1 channel revealed by electron cryomicroscopy. Proc. Natl. Acad. Sci. USA 105, 7451–7455 (2008). [PubMed: 18490661]

38. Berridge MJ, Bootman MD & Llewelyn Roderick H Calcium signalling: dynamics, homeostasis and remodelling. Nat. Rev. Mol. Cell. Bio. 4, 517–529 (2003). [PubMed: 12838335]

39. Jiang Y et al. Heterogeneous silicon mesostructures for lipid-supported bioelectric interfaces. Nat. Mater. 15, 1023–1030 (2016). [PubMed: 27348576]

40. Shapiro MG, Homma K, Villarreal S, Richter C-P & Bezanilla F Infrared light excites cells by changing their electrical capacitance. Nat. Commun. 3, 736 (2012). [PubMed: 22415827]

41. Matthes R et al. Revision of guidelines on limits of exposure to laser radiation of wavelengths between 400 nm and 1.4 μm. Health Phys. 79, 431–440 (2000). [PubMed: 11007467]

42. Chen X, Chen Y, Xin H, Wan T & Ping Y Near-infrared optogenetic engineering of photothermal nanoCRISPR for programmable genome editing. Proc. Natl. Acad. Sci. 117, 2395–2405 (2020). [PubMed: 31941712]

43. Yang X et al. Bioinspired neuron-like electronics. Nat. Mater. 18, 510–517 (2019). [PubMed: 30804509]

44. Owen SF, Liu MH & Kreitzer AC Thermal constraints on in vivo optogenetic manipulations. Nat. Neurosci. 22, 1061–1065 (2019). [PubMed: 31209378]

45. Gradinaru V et al. Targeting and readout strategies for fast optical neural control in vitro and in vivo. J. Neurosci. 27, 14231–14238 (2007). [PubMed: 18160630]

46. Lee J, Darlington TR & Lisberger SG The neural basis for response latency in a sensory-motor behavior. Cereb. Cortex 30, 3055–3073 (2020). [PubMed: 31828292]

47. Dhaka A, Viswanath V & Patapoutian A Trp ion channels and temperature sensation. Annu. Rev. Neurosci. 29, 135–161 (2006). [PubMed: 16776582]

48. Zeng X et al. Visualization of intra-neuronal motor protein transport through upconversion microscopy. Angew. Chem. Int. Ed. 58, 9262–9268 (2019).

49. Zheng W et al. Lanthanide-doped upconversion nano-bioprobes: electronic structures, optical properties, and biodetection. Chem. Soc. Rev. 44, 1379–1415 (2015). [PubMed: 25093303]

50. Zimprich A et al. A robust and reliable non-invasive test for stress responsivity in mice. Front. Behav. Neurosci. 8, 125 (2014). [PubMed: 24782732]

51. Choi C The mazes with minds of their own. Nature 555, 127–128 (2018).

52. Ibsen S, Tong A, Schutt C, Esener S & Chalasani SH Sonogenetics is a non-invasive approach to activating neurons in Caenorhabditis elegans. Nat. Commun. 6, 8264 (2015). [PubMed: 26372413]

53. Nakatsuji H et al. Thermosensitive ion channel activation in single neuronal cells by using surface-engineered plasmonic nanoparticles. Angew. Chem. Int. Ed. 54, 11725–11729 (2015).

54. Lyu Y, Xie C, Chechetka SA, Miyako E & Pu K Semiconducting polymer nanobioconjugates for targeted photothermal activation of neurons. J. Am. Chem. Soc. 138, 9049–9052 (2016). [PubMed: 27404507]

55. Lodola F, Martino N, Tullii G, Lanzani G & Antognazza MR Conjugated polymers mediate effective activation of the mammalian ion channel transient receptor potential vanilloid 1. Sci. Rep. 7, 8477 (2017). [PubMed: 28814817]

56. Li N et al. Spatiotemporal constraints on optogenetic inactivation in cortical circuits. eLife 8, e48622 (2019). [PubMed: 31736463]

57. Haas HL, Buzsaki G & International Brain Research Organization. Congress. Synaptic plasticity in the hippocampus. (Springer-Verlag, 1988).

58. Wang Y et al. Tetherless near-infrared control of brain activity in behaving animals using fully implantable upconversion microdevices. Biomaterials 142, 136–148 (2017). [PubMed: 28735174]

59. Chan KY et al. Engineered AAVs for efficient noninvasive gene delivery to the central and peripheral nervous systems. Nat. Neurosci. 20, 1172–1179 (2017). [PubMed: 28671695]

60. Madisen L et al. A toolbox of Cre-dependent optogenetic transgenic mice for light-induced activation and silencing. Nat. Neurosci. 15, 793–802 (2012). [PubMed: 22446880]

61. Chen K-T, Wei K-C & Liu H-L Theranostic strategy of focused ultrasound induced blood-brain barrier opening for CNS disease treatment. Front. Pharmacol. 10, 86 (2019). [PubMed: 30792657]

62. Su Y et al. Novel NanoLuc substrates enable bright two-population bioluminescence imaging in animals. Nat. Methods 17, 852–860 (2020). [PubMed: 32661427]

63. Lyu Y et al. Enhancing both biodegradability and efficacy of semiconducting polymer nanoparticles for photoacoustic imaging and photothermal therapy. ACS Nano 12, 1801–1810 (2018). [PubMed: 29385336]

64. Lyu Y, Xie C, Chechetka SA, Miyako E & Pu K Semiconducting polymer nanobioconjugates for targeted photothermal activation of neurons. J. Am. Chem. Soc. 138, 9049–9052 (2016). [PubMed: 27404507]

65. Zhu X et al. Temperature-feedback upconversion nanocomposite for accurate photothermal therapy at facile temperature. Nat. Commun. 7, 10437 (2016). [PubMed: 26842674]

66. Jang M, Ruan H, Judkewitz B & Yang C Model for estimating the penetration depth limit of the time-reversed ultrasonically encoded optical focusing technique. Opt. Express 22, 5787–5807 (2014). [PubMed: 24663917]

67. Martelli F, Del Bianco S. & Ismaelli A Light propagation through biological tissue and other diffusive media: theory, solutions, and software. (Society of Photo-Optical Instrumentation Engineers, 2009).

68. Yaroslavsky AN et al. Optical properties of selected native and coagulated human brain tissues in vitro in the visible and near infrared spectral range. Phys. Med. Biol. 47, 2059–2073 (2002). [PubMed: 12118601]

69. Nachabé R et al. Validation of interventional fiber optic spectroscopy with MR spectroscopy, MAS-NMR spectroscopy, high-performance thin-layer chromatography, and histopathology for accurate hepatic fat quantification. Invest. Radiol. 47, 209–216 (2012). [PubMed: 22233757]

70. PRAHL & A. S Tabulated molar extinction coefficient for hemoglobin in water. http://omlc.ogi.edu/spectra/hemoglobin/summary.html (1998).

71. Mason MG, Nicholls P & Cooper CE Re-evaluation of the near infrared spectra of mitochondrial cytochrome c oxidase: Implications for non invasive in vivo monitoring of tissues. Biochim. Biophys. Acta 1837, 1882–1891 (2014). [PubMed: 25175349]

72. Bhattacharya M & Dutta A Computational modeling of the photon transport, tissue heating, and cytochrome C oxidase absorption during transcranial near-infrared stimulation. Brain Sci. 9, (2019).

73. Welsher K, Sherlock SP & Dai H Deep-tissue anatomical imaging of mice using carbon nanotube fluorophores in the second near-infrared window. Proc. Natl. Acad. Sci. USA 108, 8943–8948 (2011). [PubMed: 21576494]

74. Jacques SL & Wang L Monte Carlo modeling of light transport in tissues. Optical-Thermal Response of Laser-Irradiated Tissue 73–100 (1995).

75. Tuchin VV Light scattering study of tissues. Phys. Usp. 167, 495–515 (1997).

76. Sabino CP et al. The optical properties of mouse skin in the visible and near infrared spectral regions. J. Photochem. Photobiol. B 160, 72–78 (2016). [PubMed: 27101274]

77. Samatham R, Phillips KG & Jacques SL Assessment of optical clearing agents using reflectance-mode confocal scanning laser microscopy. J. Innov. Opt. Health Sci. 3, 183–188 (2010).

78. Bashkatov AN & Genina EA Optical properties of human cranial bone in the spectral range from 800 to 2000 nm. Proc. SPIE 6163, 616310 (2006).

79. Ascenzi A & Fabry C Technique for dissection and measurement of refractive index of osteones. J. Biophys. Biochem. Cy. 6, 139–142 (1959).

80. Ugryumova N, Matcher SJ & Attenburrow DP Measurement of bone mineral density via light scattering. Phys. Med. Biol. 49, 469 (2004). [PubMed: 15012014]

81. Binding J et al. Brain refractive index measured in vivo with high-NA defocus-corrected full-field OCT and consequences for two-photon microscopy. Opt. Express 19, 4833–4847 (2011). [PubMed: 21445119]

82. Nathanson JL, Yanagawa Y, Obata K & Callaway EM Preferential labeling of inhibitory and excitatory cortical neurons by endogenous tropism of adeno-associated virus and lentivirus vectors. Neuroscience 161, 441–450 (2009). [PubMed: 19318117]

83. Hong G et al. Near-infrared-fluorescence-enhanced molecular imaging of live cells on gold substrates. Angew. Chem. Int. Ed. 50, 4644–4648 (2011).

84. Fu T-M et al. Stable long-term chronic brain mapping at the single-neuron level. Nat. Methods 13, 875–882 (2016). [PubMed: 27571550]

85. Lein ES et al. Genome-wide atlas of gene expression in the adult mouse brain. Nature 445, 168–176 (2007). [PubMed: 17151600]

86. Gradinaru V, Mogri M, Thompson KR, Henderson JM & Deisseroth K Optical deconstruction of parkinsonian neural circuitry. Science 324, 354–359 (2009). [PubMed: 19299587]

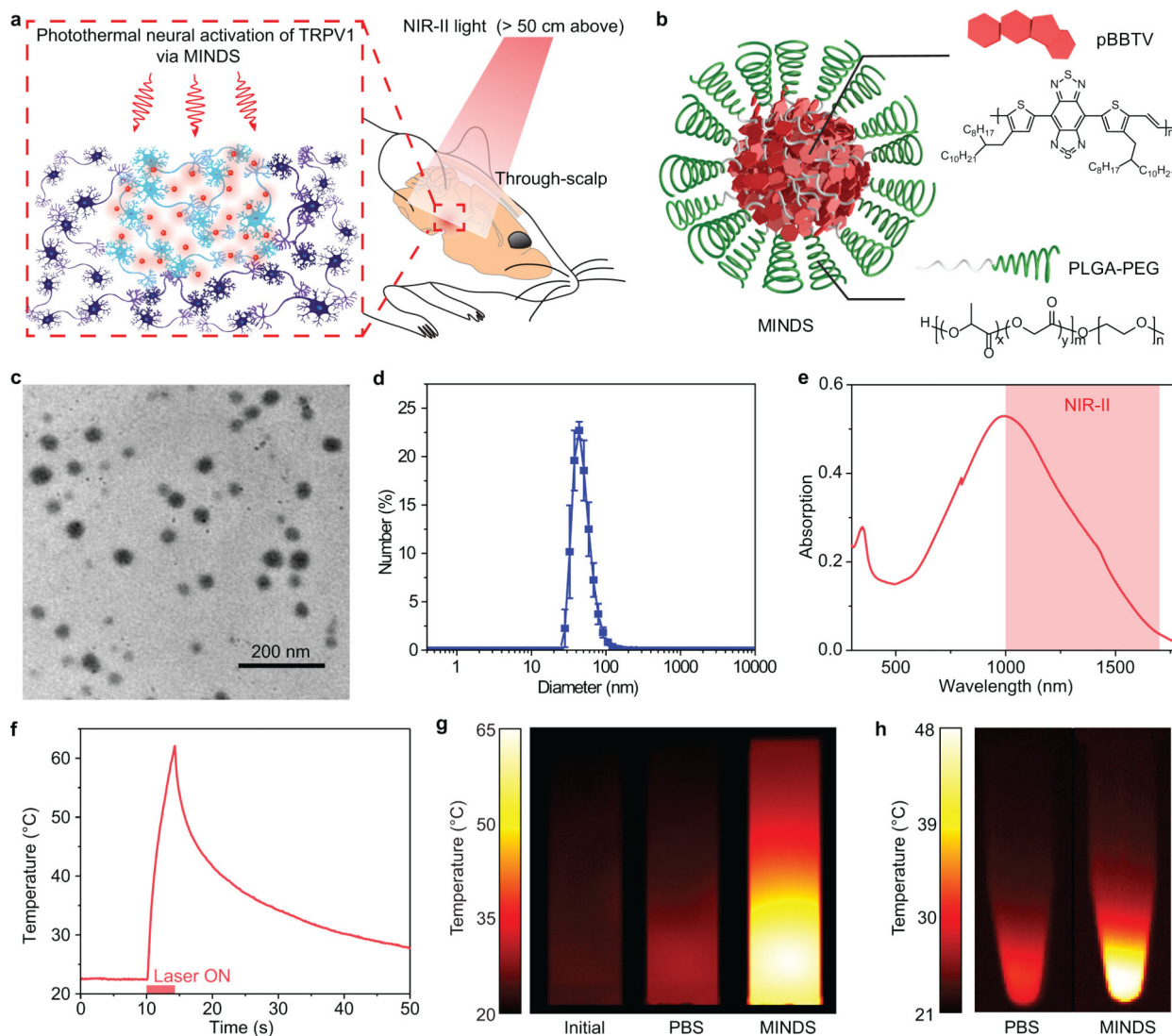87. Cohen J Statistical Power Analysis for the Behavioral Sciences. (Routledge, 2013).

Fig. 1 |. Efficient photothermal conversion of MINDS in the NIR-II window.
a, Schematic showing through-scalp neuromodulation with NIR-II illumination > 50 cm
above the mouse head, which activates TRPV1 via the sensitization of MINDS (red circles).
b, Schematic showing the composition of MINDS, highlighting the pBBTV conjugated
copolymers in the core (red hexagons) and the PLGA-PEG polymer comprising the
shell (green spirals). **c**, A representative TEM image of MINDS. The experiment was
repeated three times independently with similar results. **d**, Distribution of the hydrodynamic
diameters of MINDS revealed by DLS measurement. Data are presented as mean values
+/− standard deviation (SD). ($n = 3$ independent experiments). **e**, Absorption spectrum of
MINDS dispersion in PBS, showing strong absorption in the 1000–1700 nm NIR-II window
(red shade). **f**, Representative photothermal heating and cooling curve of 1.8 mg mL^{-1}
MINDS dispersion, where the red bar indicates illumination with a 1064-nm laser at a power
density of 10 mW mm^{-2}. **g**, Thermal images showing efficient photothermal heating of 25
μg mL^{-1} MINDS (right), in comparison with the same solution before NIR-II illumination
(left) and PBS (middle). Both the PBS and MINDS images were taken when the temperature

reached equilibrium after 30 min under 10 mW mm^{-2} 1064-nm illumination. **h**, Thermal images of cell pellets incubated with PBS and MINDS, showing effective heating of cells with MINDS. Both images were taken when the temperature of the cell pellet reached equilibrium after 10 min under 10 mW mm^{-2} 1064-nm illumination.
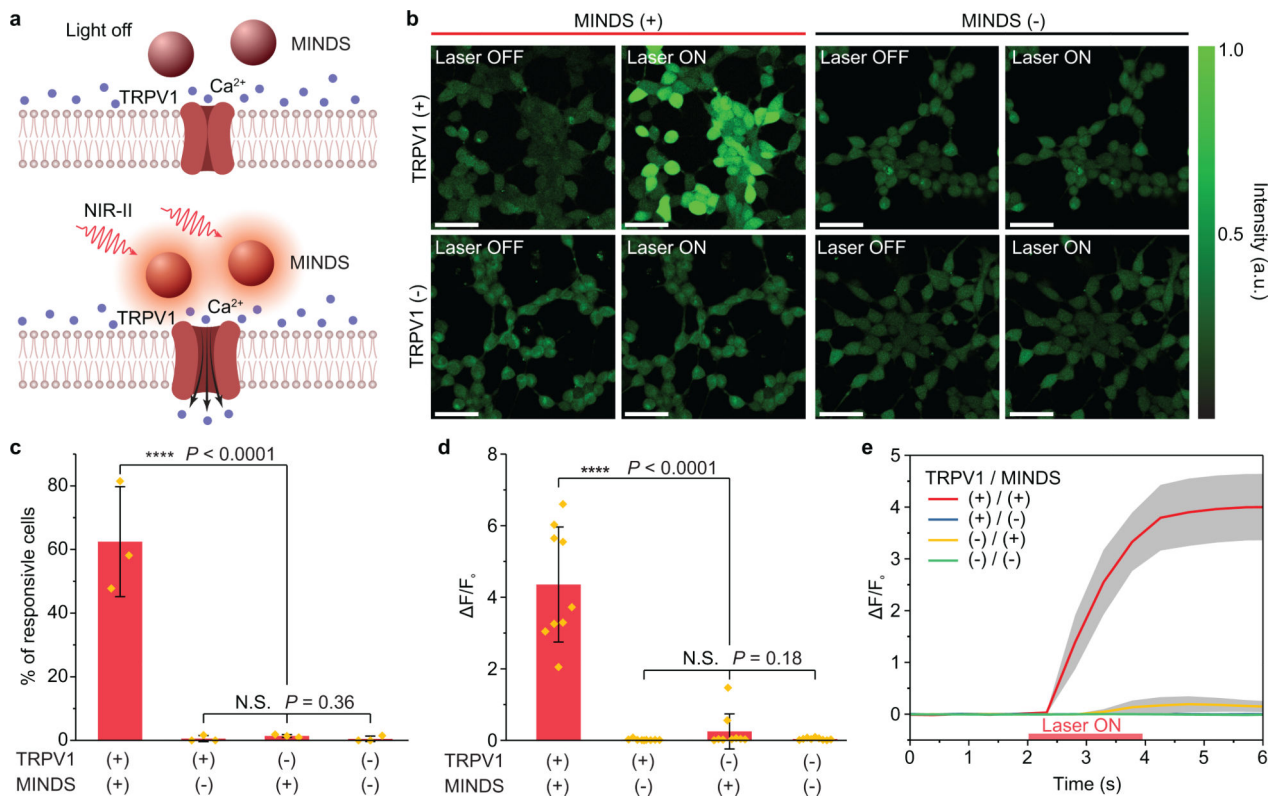
Fig. 2 |. NIR-II photothermal activation of MINDS-sensitized TRPV1 *in vitro*.
a, Schematic showing NIR-II photothermal activation of TRPV1 expressed in the plasma membrane of cells mediated by MINDS. **b**, Calcium imaging of HEK293T cells under different experimental conditions. A calcium signal increase is only seen when the NIR-II laser illuminates TRPV1+/MINDS+ cells. The experiment was repeated three times independently with similar results. Scale bars represent 50 μm. **c**, Percentage of responsive cells upon NIR-II illumination. A cell is defined responsive if its calcium signal rises over 50% of original intensity within 5 s of NIR-II illumination (i.e., $F/F_0 > 50\%$)[25]. ($n = 3$ independent experiments for each group, including 874 cells in total; one-way analysis of variance (ANOVA), $F_{(3,8)} = 38$, $P < 0.0001$; $F_{(2,6)} = 1.23$, $P = 0.36$). Data are presented as mean values +/− SD. **d**, Statistical analysis of calcium signal changes for different groups of cells ($n = 9$ replicates with 15 cells in each replicate), shown as the ratio of maximum calcium signal change after NIR-II illumination over the original calcium signal before NIR-II illumination. (One-way ANOVA, $F_{(3,32)} = 40.74$, $P < 0.0001$; $F_{(2,24)} = 1.82$, $P = 0.18$). Data are presented as mean values +/− SD. **e**, Temporal dynamics of the calcium signal for different groups of cells, showing an average latency time of 0.9 ± 0.2 s for calcium signal to increase over 3 SD of baseline and 1.1 ± 0.2 s to increase to 50% of the maximum. Data are presented as mean values +/− standard error of the mean ($n = 9$ replicates with 15 cells in each replicate). (P 0.05 (N.S.), ****$P < 0.0001$. N.S., not significant.)
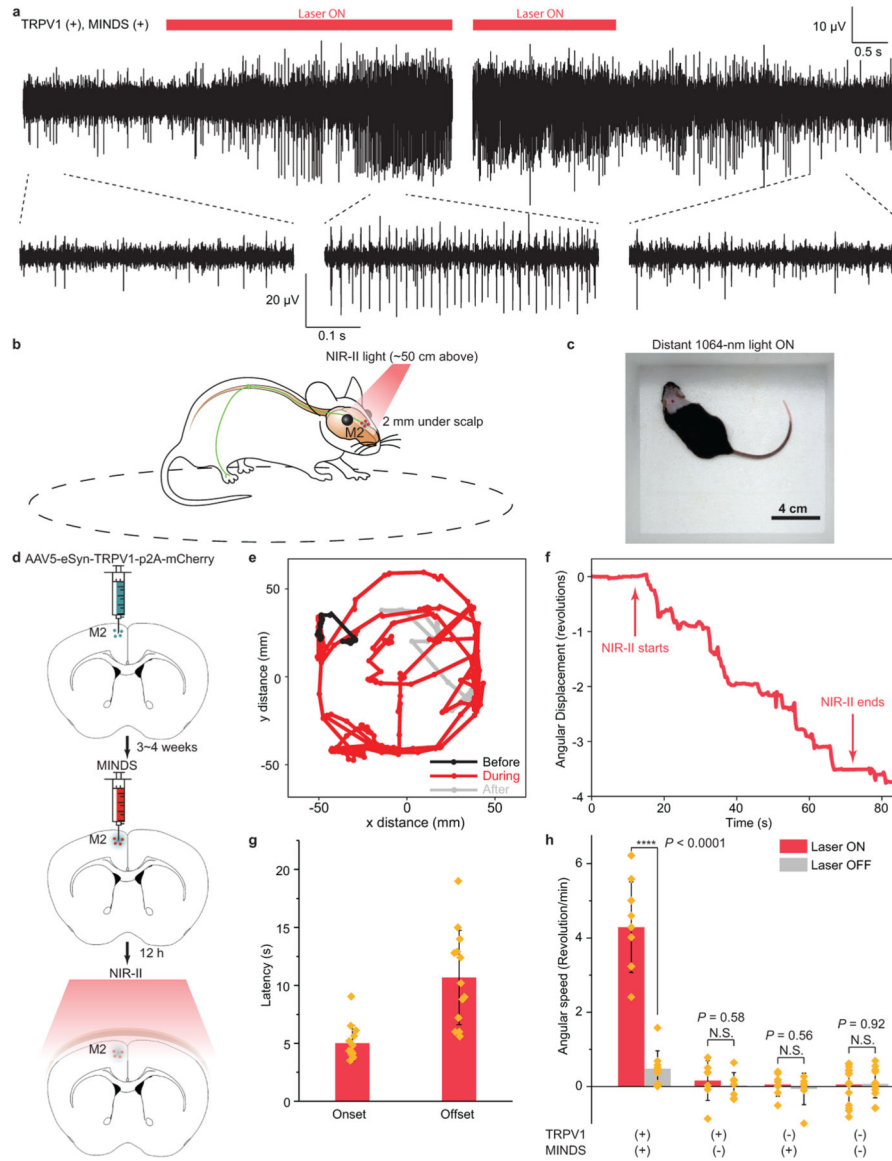
Fig. 3 |. Through-scalp NIR-II neuromodulation of the mouse hippocampus and motor cortex.
a, Representative traces showing the increase in neuron firing rate in the mouse hippocampus upon 1064-nm light illumination (left). The neuron firing rate returned to the baseline after the 1064-nm light was turned off (right). **b**, Schematic showing through-scalp NIR-II activation of motor neurons (located ca. 2 mm underneath scalp surface) that ectopically overexpress TRPV1 channels and project to the spinal cord for controlling the unilateral limb via the sensitization of MINDS (red dots). **c**, A representative image showing the arena for motor behavioural modulation by distant NIR-II illumination (invisible in the image since the camera used to take this image is insensitive to the NIR-II wavelength). **d**, Schematics illustrating the process of TRPV1 virus delivery (green dots, top), injection of MINDS (red dots, middle, where the green haze indicates neural tissue transduced with TRPV1), and NIR-II activation of TRPV1 neurons through the scalp (bottom). **e**, Trajectory of the mouse before (black), during (red) and after (gray) distant NIR-II illumination. **f**,

Angular displacement (number of revolutions, where positive indicates counter-clockwise revolutions and negative indicates clockwise revolutions) before, during and after NIR-II illumination. **g**, Bar chart showing the statistics of onset and offset latency times for M2 neural stimulation with NIR-II illumination. See Methods for the definitions of onset and offset latency times. Data are presented as mean values +/− SD and each point indicates an independent trial from a total of $N = 13$ trials. **h**, Statistical analysis of rotational movements of animals under different experimental conditions. ($n = 6$ mice for TRPV1+/MINDS+ and $n = 3$ mice for all other groups; one-way ANOVA, $F(1,16) = 76.13$, $P < 0.0001$; $F(1,12) = 0.32$, $P = 0.58$; $F(1,12) = 0.36$, $P = 0.56$; $F(1,26) = 0.01$, $P = 0.92$). Data are presented as mean values +/− SD and each point indicates an independent trial. (P 0.05 (N.S.), ****$P < 0.0001$.)
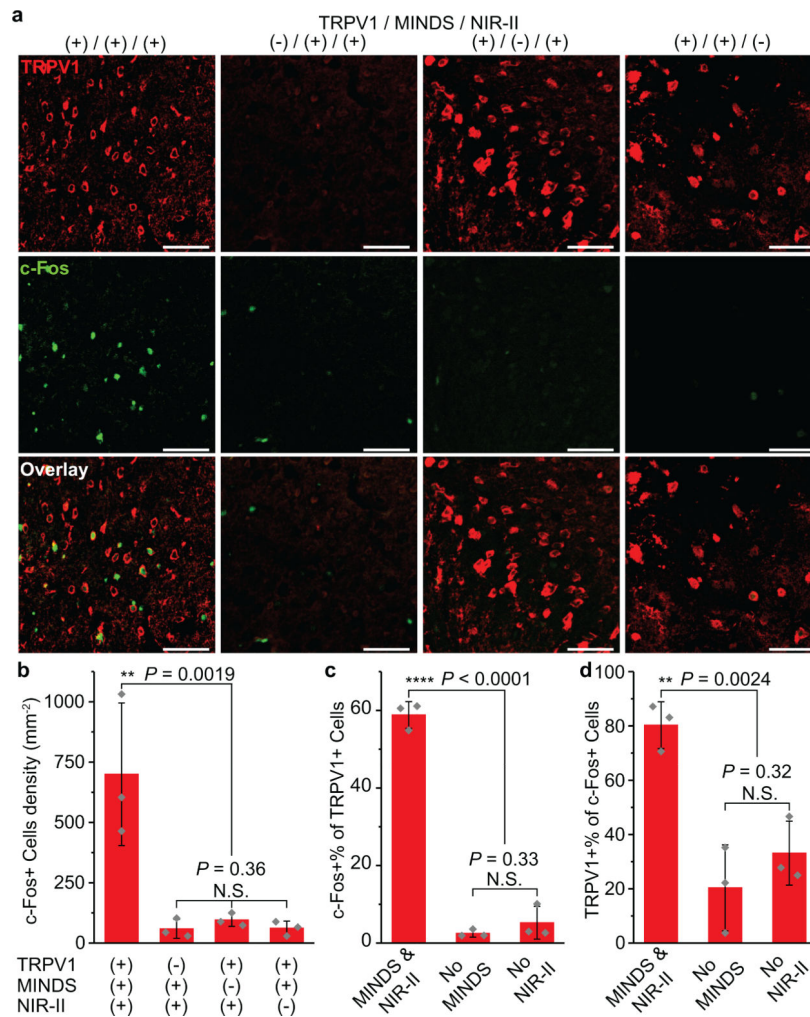
Fig. 4 |. Immunohistology of the M2 region after NIR-II illumination.
a, Confocal images of the M2 region under different experiment conditions. An increase in c-Fos expression driven by NIR-II stimulation was only observed in the presence of both TRPV1 and MINDS. The scale bars indicate 50 μm. The number of images taken is reflected in the n values for **b–d**. **b**, Statistical analysis for the density of c-Fos+ cells for the four experiment conditions in **a** (one-way ANOVA, $F(3,8) = 13.11$, $P = 0.0019$; $F(2,6) = 1.22$, $P = 0.36$). **c**, Percentage of c-Fos+ cells within the TRPV1+ cell population. (one-way ANOVA, $F(2,6) = 296.45$, $P < 0.0001$; $F(1,4) = 1.2$, $P = 0.33$). **d**, Percentage of TRPV1+ cells within the c-Fos+ cell population. (one-way ANOVA, $F(2,6) = 19.32$, $P < 0.0024$; $F(1,4) = 1.26$, $P = 0.32$). Both **c** and **d** were analysed for the three experimental groups with TRPV1 transduction. All data are presented as mean values +/− SD $n = 3$ mice per group (P 0.05 (N.S.), **$P < 0.01$, ****$P < 0.0001$.).
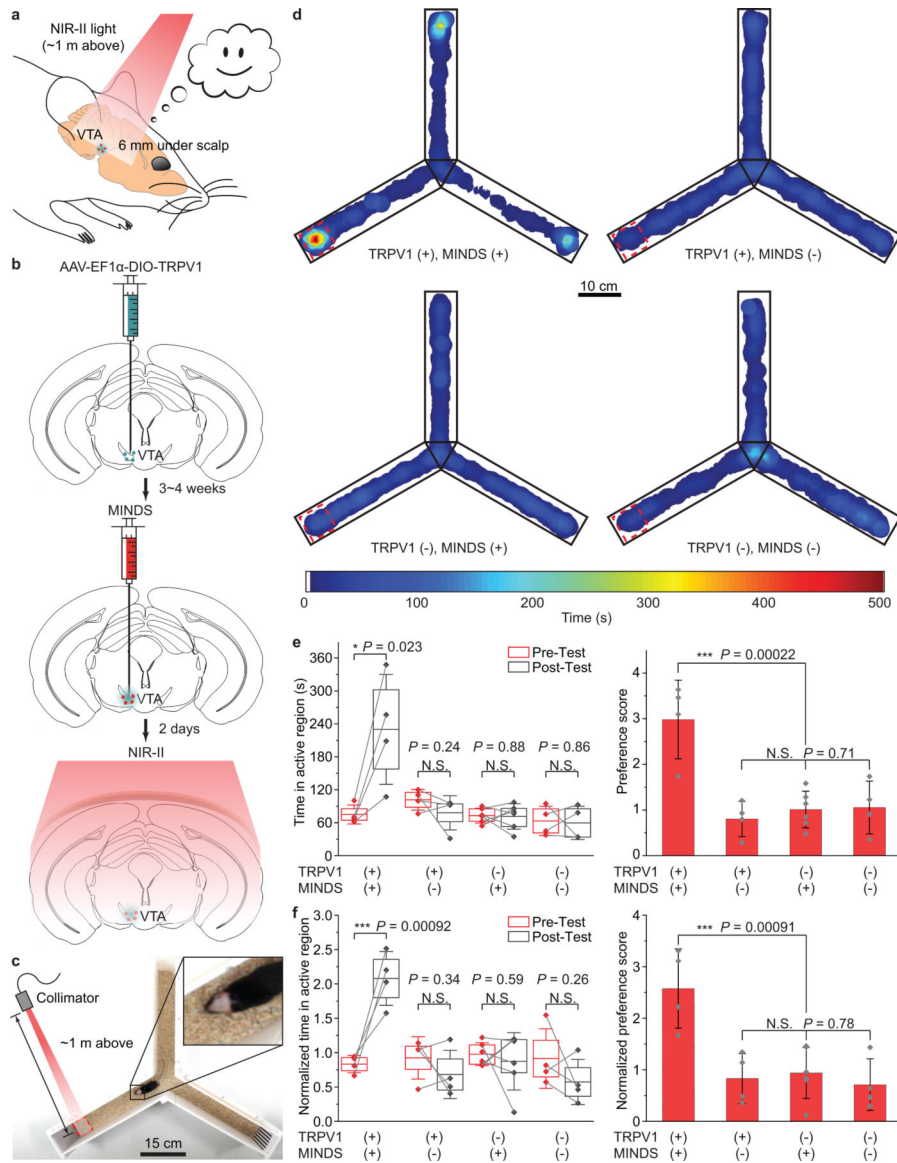
Fig. 5 |. Through-scalp NIR-II stimulation of a deep-brain region.
a, Schematic showing through-scalp NIR-II activation of VTA dopaminergic neurons (located ca. 6 mm underneath the scalp surface) that ectopically express TRPV1 via the sensitization of MINDS (red dots). **b**, Schematics illustrating the process of the specific transduction of dopaminergic neurons with TRPV1 (green dots, left), injection of MINDS (red dots, middle, where the green haze indicates neural tissue transduced with TRPV1), and distant NIR-II illumination for neural modulation through the scalp (right). **c**, Photograph showing the setup of a Y-maze for contextual conditioning test. **d**, Representative post-test heat maps showing the time of travel of mice under different experimental conditions. Red dashed squares indicate NIR-II irradiated regions. **e**, Statistical analysis of time spent in the NIR-II illuminated region (left) and preference score (right) for different TRPV1/MINDS combinations in the VTA. (One-way ANOVA, left: $F(1,6) = 9.29$, $P = 0.023$; $F(1,6) = 1.69$, $P = 0.24$; $F(1,10) = 0.02$, $P = 0.88$; $F(1,6) = 0.03$, $P = 0.86$; right: $F(3,14) = 13.35$, $P =$

0.00022; $F_{(2,11)}$ = 0.36, P = 0.71.) **f**, Statistical analysis of the normalized time spent in the NIR-II illuminated region (left) and the normalized preference score (right) for different TRPV1/MINDS combinations in the VTA. (One-way ANOVA, left: $F_{(1,6)}$ = 36.67, P = 0.00092; $F_{(1,6)}$ = 1.07, P = 0.34; $F_{(1,10)}$ = 0.32, P = 0.59; $F_{(1,6)}$ = 1.57, P = 0.26; right: $F_{(3,14)}$ = 9.93, P = 0.00091; $F_{(2,11)}$ = 0.25, P = 0.78.) See Methods for the definitions of preference score, normalized time in the active region and normalized preference score. In the left panels of both **e** and **f**, the centre lines, lower bound, upper bound, and whiskers indicate the mean, 25th percentile, 75th percentile, and ±1 SD, respectively. In the right panels of **e** and **f**, data are presented as mean values +/− SD. n = 6 mice for TRPV1–/ MINDS+ and n = 4 mice for all other groups, with data points shown for each animal. (P 0.05 (N.S.), *P < 0.05, ***P < 0.001.)
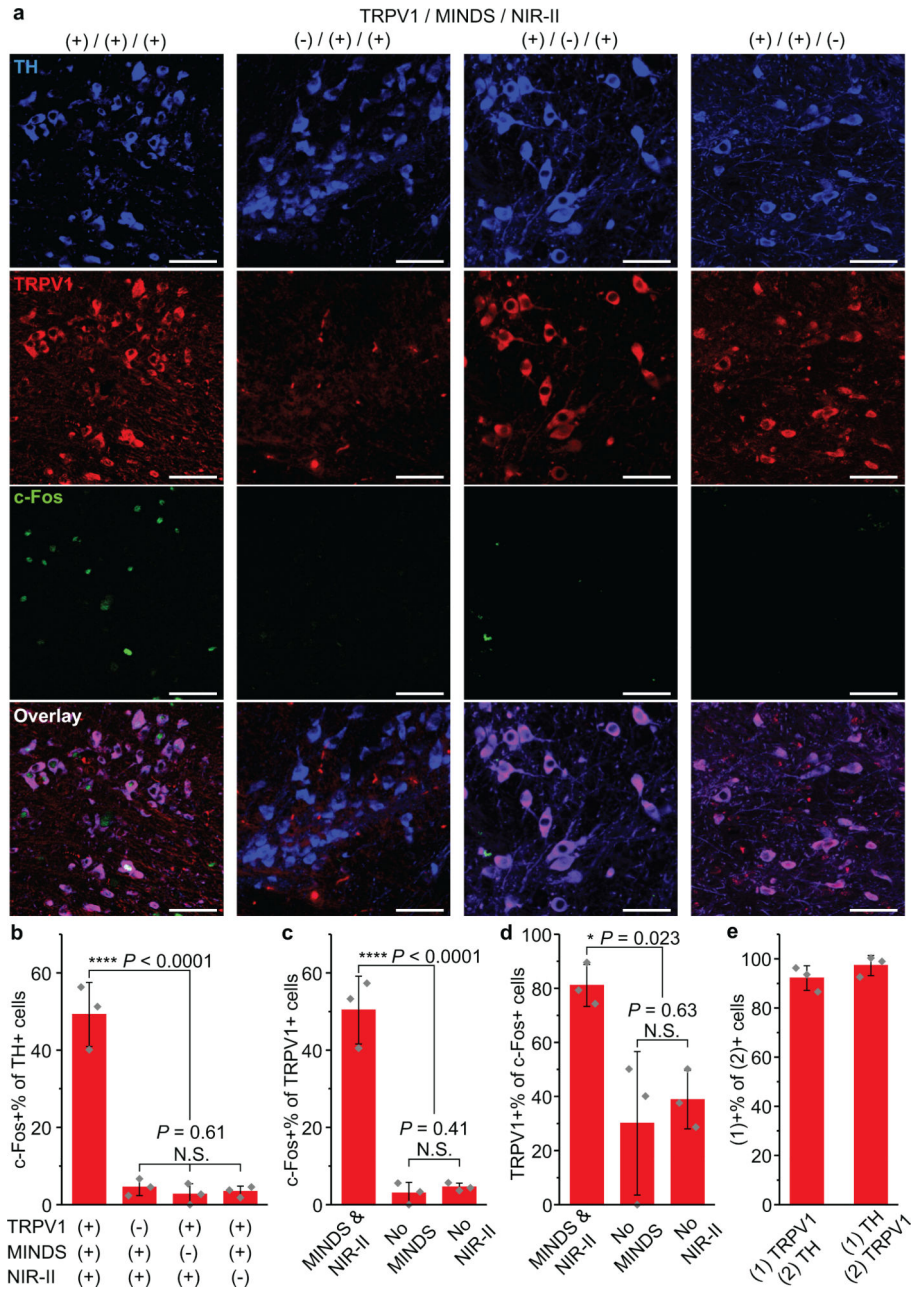
Fig. 6 |. Immunohistology of the VTA region after NIR-II illumination.
a, Confocal images of the VTA region under different experimental conditions. An increase in c-Fos expression driven by NIR-II stimulation was only observed in the presence of both TRPV1 and MINDS. The scale bars indicate 50 μm. The number of images taken is reflected in the n values for **b–d**. **b**, Percentage of c-Fos+ neurons in the TH+ cell population, corresponding to the four conditions presented in **a**. (One-way ANOVA, $F_{(3,8)}$ = 75.69, $P < 0.0001$; $F_{(2,6)} = 0.54$, $P = 0.61$.) **c**, Percentage of c-Fos+ cells within the TRPV1+ cell population. (One-way ANOVA, $F_{(2,6)} = 75.83$, $P < 0.0001$; $F_{(1,4)} = 0.85$, $P = 0.41$.) **d**, Percentage of TRPV1+ cells within the c-Fos+ cell population. Both **c** and **d** were analysed for the three experimental groups with TRPV1 transduction. (One-way ANOVA,

$F_{(2,6)} = 7.59$, $P = 0.023$; $F_{(1,4)} = 0.28$, $P = 0.63$.) **e**, Statistics of TRPV1 expression in TH+ neurons (left bar) and TH expression in TRPV1+ neurons (right bar). All data are presented as mean values +/− SD ($n = 3$ mice per group, P 0.05 (N.S.), $*P < 0.05$, $****P < 0.0001$).